IOPscience iopscience.iop.org

Home Search Collections Journals About Contact us My IOPscience

Analysis of the Hessian for inverse scattering problems: I. Inverse shape scattering of acoustic waves

This article has been downloaded from IOPscience. Please scroll down to see the full text article.

2012 Inverse Problems 28 055001

(http://iopscience.iop.org/0266-5611/28/5/055001)

View the table of contents for this issue, or go to the journal homepage for more

Download details:
IP Address: 128.83.68.73
The article was downloaded on 05/04/2012 at 07:31

Please note that terms and conditions apply.

Inverse Problems **28** (2012) 055001 (32pp) doi:10.1088/0266-5611/28/5/055001

Analysis of the Hessian for inverse scattering problems: I. Inverse shape scattering of acoustic waves

Tan Bui-Thanh[1] **and Omar Ghattas**[1,2,3]

[1] Institute for Computational Engineering and Sciences, The University of Texas at Austin, Austin, TX 78712, USA
[2] Jackson School of Geosciences, The University of Texas at Austin, Austin, TX 78712, USA
[3] Department of Mechanical Engineering, The University of Texas at Austin, Austin, TX 78712, USA

E-mail: tanbui@ices.utexas.edu and omar@ices.utexas.edu

Received 20 June 2011
Published 4 April 2012
Online at stacks.iop.org/IP/28/055001

Abstract

We derive expressions for the shape Hessian operator of the data misfit functional corresponding to the inverse problem of inferring the shape of a scatterer from reflected acoustic waves, using a Banach space setting and the Lagrangian approach. The shape Hessian is then analyzed in both Hölder and Sobolev spaces. Using an integral equation approach and compact embeddings in Hölder and Sobolev spaces, we show that the shape Hessian can be decomposed into four components, of which the Gauss–Newton part is a compact operator, while the others are not. Based on the Hessian analysis, we are able to express the eigenvalues of the Gauss–Newton Hessian as a function of the smoothness of the shape space, which shows that the smoother the shape is, the faster the decay rate. Analytical and numerical examples are presented to validate our theoretical results. The implication of the compactness of the Gauss–Newton Hessian is that for small data noise and model error, the discrete Hessian can be approximated by a low-rank matrix. This in turn enables fast solution of an appropriately regularized inverse problem, as well as Gaussian-based quantification of uncertainty in the estimated shape.

(Some figures may appear in colour only in the online journal)

1. Introduction

A feature of many ill-posed inverse problems is that the Hessian operator of the data misfit functional is a compact operator with rapidly decaying eigenvalues. This is a manifestation of the typically sparse observations, which are informative about a limited number of modes of the infinite-dimensional field we seek to infer. The Hessian operator (and its finite-dimensional discretization) play an important role in the analysis and solution of the inverse problem. In particular, the spectrum of the Hessian at the solution of the inverse problem determines the degree of ill-posedness and provides intuition on the construction of appropriate regularization

 © 2012 IOP Publishing Ltd Printed in the UK & the USA

strategies. This has been observed, analyzed and exploited in several applications including shape optimization [1, 2] and inverse wave propagation [3–5], to name a few.

Moreover, solution of the inverse problem by the gold standard iterative method—Newton's method—requires 'inversion' of the Hessian at each iteration. Compactness of the Hessian of the data misfit functional accompanied by sufficiently fast eigenvalue decay permits a low rank approximation, which in turn facilitates rapid inversion or preconditioning of the regularized Hessian [3, 6]. Alternatively, the solution of the linear system arising at each Newton iteration by a conjugate gradient method can be very fast if the data misfit Hessian is compact with rapidly decaying eigenvalues and the conjugate gradient iteration is preconditioned by the regularization operator [7]. Finally, under a Gaussian approximation to the Bayesian solution of the inverse problem, the covariance of the posterior probability distribution is given by the inverse of the Hessian of the negative log likelihood function. For Gaussian data noise and model error, this Hessian is given by an appropriately weighted Hessian of the data misfit operator, e.g. [8]. Here again, exploiting the low-rank character of the data misfit component of the Hessian is critical for rapidly approximating its inverse, and hence the uncertainty in the inverse solution [4, 5, 9, 10].

In all of the cases described above, compactness of the data misfit Hessian is a critical feature that enables fast solution of the inverse problem, scalability of solvers to high dimensions and estimation of uncertainty in the solution. With this motivation, here we analyze the shape Hessian operator for inverse acoustic shape scattering problems, and study its compactness. Our analysis is based on an integral equation formulation of the Helmholtz equation, adjoint methods and compact embeddings in Hölder and Sobolev spaces. These tools allow us to state the shape derivatives in a Banach space setting, and then to analyze the shape Hessian in detail. In particular, the Gauss–Newton component of the full Hessian is shown to be a compact operator, and the decay rate of its eigenvalues is quantified as a function of the shape smoothness. Furthermore, under certain conditions, the eigenvalues can be shown to decay exponentially.

The remainder of the paper is organized as follows. Section 2 briefly derives and formulates two-dimensional forward and inverse shape acoustic scattering problems, followed by section 3 on a general framework for shape derivatives in a Banach space setting. Using the results in section 3 and a Lagrangian approach, we then derive shape derivatives for the inverse shape scattering problem in section 4. Section 5 justifies the shape derivations by studying the well-posedness of the (incremental) forward and (incremental) adjoint equations, and the regularity of their solutions. Next, we analyze the shape Hessian in Hölder spaces in section 6, and then extend the analysis to Sobolev spaces in section 7. Section 8 expresses the decay rate of the eigenvalues of the Gauss–Newton component in terms of the shape smoothness. In order to validate our theoretical developments, we give analytical as well as numerical examples in sections 9 and 10. Finally, the conclusions of the paper are presented in section 11, and straightforward extensions of two-dimensional results to three dimensions are discussed in the appendix.

2. Forward and inverse shape scattering formulations

2.1. Forward shape scattering formulation

For simplicity of exposition, we will exclusively work with the two-dimensional setting; extensions to three dimensions will be presented in the appendix. We further assume that the scatterer Ω_S (for convenience, one scatterer is considered, but all the results in this paper hold true for multiple scatterers) under consideration is *sound-soft*. If the incident wave is a

plane wave, we can eliminate the time harmonic factor $e^{-i\omega t}$, where $i^2 = -1$, and the acoustic scattering problem can be cast into the following exterior Helmholtz equation [11]:

$$\nabla^2 U + k^2 U = 0 \quad \text{in } \Omega, \tag{1a}$$

$$U = -U^I \quad \text{on } \Gamma_s, \tag{1b}$$

$$\lim_{r\to\infty} \sqrt{r}\left(\frac{\partial U}{\partial r} - ikU\right) = 0, \tag{1c}$$

where k is the wave number, U the scattered field, U^I the incident field which is assumed to be an entire solution of the Helmholtz equation (1*a*), Ω the exterior domain given by $\Omega = \mathbb{R}^2 \setminus \overline{\Omega}_S$ and (1*c*) the radiation condition which is assumed to be valid uniformly in all directions $\frac{\mathbf{x}}{\|\mathbf{x}\|}$.

We have derived the governing equations (1) for two-dimensional acoustic scattering under time harmonic incident wave assumption. It turns out that two-dimensional electromagnetic scattering on perfect electric conducting obstacles is governed by the same set of equations. Consequently, all the results in this paper are valid for both acoustic and electromagnetic scattering problems in two dimensions.

2.2. Inverse shape scattering formulation

For the inverse problem, the task is to reconstruct the scatterer's shape given scattered field data observed at some parts of the domain. For simplicity in the following analysis, the observed scattering data are assumed to be noise-free.

The inverse task can be formulated as the following PDE-constrained shape optimization problem:

$$\min_{\Omega_S} \mathcal{J} = \int_\Omega K(\mathbf{x}) |U - U^{\text{obs}}|^2 \, d\Omega \tag{2}$$

subject to

$$\nabla^2 U + k^2 U = 0 \quad \text{in } \Omega, \tag{3a}$$

$$U = -U^I \quad \text{on } \Gamma_s, \tag{3b}$$

$$\lim_{r\to\infty} \sqrt{r}\left(\frac{\partial U}{\partial r} - ikU\right) = 0, \tag{3c}$$

where quantities with superscript 'obs' are the observed data. $K(\mathbf{x})$ denotes the observation operator with compact support and $\operatorname{supp} K \subset \Omega$. We identify

$$\mathcal{K}\varphi = \int_\Omega K\varphi \, d\Omega = \int_\Omega \mathbf{1}_{\operatorname{supp} K} \varphi \, d\Omega,$$

where $\mathbf{1}_{\operatorname{supp} K}$ is the characteristic function of the set $\operatorname{supp} K$. In particular, if the measurements are pointwise at $\mathbf{x}_j^{\text{obs}}$, $j = 1, \ldots, N^{\text{obs}}$, we have

$$\mathcal{K}\varphi = \int_\Omega K\varphi \, d\Omega = \sum_{j=1}^{N^{\text{obs}}} \varphi\left(\mathbf{x}_j^{\text{obs}}\right).$$

For simplicity in writing, we define $\Gamma_b = \operatorname{supp} K$.

3. Shape derivatives in a Banach space setting

If we restrict our attention to a special shape space which is Banach, the shape calculus becomes the usual differential calculus on Banach spaces and many interesting conclusions can be drawn. As we will see in what follows, only Fubini's theorem and Leibniz' rule are necessary to derive the first and second order shape derivatives in this setting.

Following [12, 13], we represent the shape by its boundary. In particular, we assume that the scatterer $\Omega_S \subsetneq \mathbb{R}^2$ is a simply connected domain and starlike with respect to the origin. Thus, its boundary $\partial\Omega_S$ can be parametrized as

$$\partial\Omega_S \equiv \Gamma_s = \{\mathbf{r} = r(\theta)\,\mathbf{e}_r : \theta \in [0, 2\pi]\}, \quad \mathbf{e}_r = [\cos\theta, \sin\theta]^T. \tag{4}$$

We assume that Γ_s belongs to the Hölder continuous class $C^{m,\alpha}$ for $0 < \alpha \leqslant 1$. That is, the radius r lives in the Hölder continuous space $C^{m,\alpha}([0, 2\pi])$ with the periodic condition

$$r^{(j)}(0) = r^{(j)}(2\pi), \quad j = 0, \ldots, m, \tag{5}$$

where the superscript (j) denotes the jth derivative with respect to θ. To the end of the paper, unless otherwise stated, functions defined on $[0, 2\pi]$ are periodic in the sense of (5).

We are now in the position to derive the shape derivatives. For the purpose of this paper, it suffices to consider the first order shape derivative of the following functional:

$$\mathcal{I} = \int_\Omega f(\mathbf{x})\,\mathrm{d}\Omega. \tag{6}$$

The following lemma provides the shape derivatives of $\mathcal{I}$ that will be used later in the derivation of the shape Hessian for our inverse shape scattering problems (an analogous result for interior problems can be found in [13]).

Lemma 1. *Assume that $f \in C^1(\mathbb{R}^2)$; then, $\mathcal{I}$ is twice continuously Fréchet differentiable for all $r \in C^1([0, 2\pi])$, and its shape derivatives are given as*

$$D\mathcal{I}(r;\hat{r}) = -\int_0^{2\pi} f r\hat{r}\,\mathrm{d}\theta = -\int_{\Gamma_s} f\frac{r\hat{r}}{\sqrt{r^2 + r'^2}}\,\mathrm{d}s, \tag{7a}$$

$$D^2\mathcal{I}(r;\hat{r},\tilde{r}) = -\int_0^{2\pi}\left(\frac{\partial f}{\partial \mathbf{e}_r} + \frac{f}{r}\right) r\hat{r}\tilde{r}\,\mathrm{d}\theta = -\int_{\Gamma_s}\left(\frac{\partial f}{\partial \mathbf{e}_r} + \frac{f}{r}\right)\frac{r\hat{r}\tilde{r}}{\sqrt{r^2 + r'^2}}\,\mathrm{d}s \tag{7b}$$

for all $\hat{r}, \tilde{r} \in C^1([0, 2\pi])$.

Proof. We use the Leibniz rule to compute the first Gâteaux variation to obtain the shape derivative formulas (7*a*) and (7*b*). Then, it is obvious that both $D\mathcal{I}(r;\hat{r})$ and $D^2\mathcal{I}(r;\hat{r},\tilde{r})$ are linear and continuous with respect to $\hat{r}$ (and $\tilde{r}$). Now the continuity of $D\mathcal{I}(r;\hat{r})$ and $D^2\mathcal{I}(r;\hat{r},\tilde{r})$ with respect to r is straightforward owing to $f \in C^1(\mathbb{R}^2)$. Hence, a classical result on sufficiency for the Fréchet derivative [14] ends the proof. □

4. Shape derivative derivations for inverse wave scattering problems

In this section, we derive the shape gradient and shape Hessian using a reduced space approach, and the justifications for our derivations are provided in the next section. We begin with a useful observation on the radiation condition. Since the radiation condition (1*c*) is valid uniformly in all directions $\frac{\mathbf{x}}{\|\mathbf{x}\|}$, we rewrite the radiation condition as

$$\frac{\partial U}{\partial r} - \mathrm{i}kU = \varphi(r) = o(r^{-1/2}),$$

where r is the radius of a sufficiently large circle Γ_∞.

It can be seen that the cost functional (2) is real-valued while the constraints (3*a*)–(3*c*) are complex-valued. Consequently, the usual Lagrangian approach will not make sense and care must be taken. Following Kreutz-Delgado [15], we define the Lagrangian as

$$\begin{aligned}\mathcal{L} = \mathcal{J} &+ \int_\Omega \overline{u}(\nabla^2 U + k^2 U)\,\mathrm{d}\Omega + \int_{\Gamma_s} \overline{u}_s \left(U + U^I\right)\,\mathrm{d}s + \int_{\Gamma_\infty} \overline{u}_r \left(\frac{\partial U}{\partial r} - \mathrm{i}kU - \varphi\right)\mathrm{d}s \\ &+ \int_\Omega u(\nabla^2 \overline{U} + k^2 \overline{U})\,\mathrm{d}\Omega + \int_{\Gamma_s} u_s(\overline{U} + \overline{U}^I)\,\mathrm{d}s + \int_{\Gamma_\infty} u_r \left(\frac{\partial \overline{U}}{\partial r} + \mathrm{i}k\overline{U} - \overline{\varphi}\right)\mathrm{d}s,\end{aligned} \tag{8}$$

where the overline, when acting on forward and adjoint states (and their variations), denotes the complex conjugate.

Taking the first variation of the Lagrangian with respect to u, u_s, u_r in the directions $\hat{u}, \hat{u}_s, \hat{u}_r$ and arguing that the variations $\hat{u}, \hat{u}_s, \hat{u}_r$ are arbitrary yield the forward equations (3*a*)–(3*c*).

Now taking the first variation of the Lagrangian with respect to U and arguing that its variation $\hat{U}$ is arbitrary yields the following adjoint equations:

$$\nabla^2 u + k^2 u = -K\,(U - U^m) \quad \text{in } \Omega, \tag{9a}$$

$$u = 0 \text{ on } \quad \Gamma_s, \tag{9b}$$

$$\lim_{r\to\infty} \sqrt{r}\left(\frac{\partial u}{\partial r} + \mathrm{i}ku\right) = 0. \tag{9c}$$

The other adjoint variables are found to be

$$u_s = \frac{\partial u}{\partial \mathbf{n}} \quad \text{on } \Gamma_s, \quad \text{and} \quad u_r = -u \quad \text{on } \Gamma_\infty,$$

and they are eliminated so that the Lagrangian now becomes

$$\begin{aligned}\mathcal{L} = \mathcal{J} &+ \int_\Omega \overline{u}(\nabla^2 U + k^2 U) + \nabla\cdot\left[\left(U + U^I\right)\nabla\overline{u}\right]\mathrm{d}\Omega \\ &- \int_{\Gamma_\infty} \overline{u}\left(\frac{\partial U}{\partial r} - \mathrm{i}kU - \varphi\right)\mathrm{d}s - \int_{\Gamma_\infty} \left(U + U^I\right)\frac{\partial \overline{u}}{\partial r}\,\mathrm{d}s \\ &+ \int_\Omega u\left(\nabla^2\overline{U} + k^2\overline{U}\right) + \nabla\cdot\left[\left(\overline{U} + \overline{U}^I\right)\nabla u\right]\mathrm{d}\Omega \\ &- \int_{\Gamma_\infty} u\left(\frac{\partial \overline{U}}{\partial r} + \mathrm{i}k\overline{U} - \overline{\varphi}\right)\mathrm{d}s - \int_{\Gamma_\infty} \overline{(U + U^I)}\frac{\partial u}{\partial r}\,\mathrm{d}s.\end{aligned} \tag{10}$$

Now the shape derivative of the Lagrangian (10) can be obtained using formula (7*a*), i.e.

$$D\mathcal{J}(r;\hat{r}) = -\int_0^{2\pi} [\nabla(U + U^I)\cdot\nabla\overline{u} + \nabla(\overline{U} + \overline{U}^I)\cdot\nabla u] r\hat{r}\,\mathrm{d}\theta, \tag{11}$$

where the boundary conditions for both forward and adjoint states on the scatterer's surface have been used to lead to (11).

For the sake of convenience in deriving the shape Hessian, the state and adjoint equations are best expressed in the weak form. As a direct consequence of the above variational calculus steps, the weak form of the forward problem reads

$$\begin{aligned}\mathcal{S}(r, U) = &\int_\Omega \overline{\hat{u}}(\nabla^2 U + k^2 U) + \nabla\cdot[(U + U^I)\nabla\overline{\hat{u}}]\,\mathrm{d}\Omega \\ &- \int_{\Gamma_\infty} \overline{\hat{u}}\left(\frac{\partial U}{\partial r} - \mathrm{i}kU - \varphi\right)\mathrm{d}s - \int_{\Gamma_\infty} (U + U^I)\frac{\partial \overline{\hat{u}}}{\partial r}\,\mathrm{d}s = 0, \quad \forall\hat{u},\end{aligned} \tag{12}$$

and similarly for the adjoint problem we have

$$\mathcal{T}(r,U,u) = \int_\Omega \overline{\hat{U}}\left[\nabla^2 u + k^2 u + K(U-U^m)\right] + \nabla\cdot\left(u\nabla\overline{\hat{U}}\right)\,\mathrm{d}\Omega - \int_{\Gamma_\infty}\overline{\hat{U}}\left(\frac{\partial u}{\partial r} + \mathrm{i}ku\right)\mathrm{d}s - \int_{\Gamma_\infty} u\frac{\partial\overline{\hat{U}}}{\partial r}\,\mathrm{d}s = 0, \quad \forall\hat{U}. \tag{13}$$

Next, the shape Hessian is obtained by simply computing the first variation of the shape gradient $D\mathcal{J}\left(r;\hat{r}\right)$ using the shape derivative formula (7*b*), i.e.

$$\begin{aligned} D^2\mathcal{J}(r;\hat{r},\tilde{r}) = &-\int_0^{2\pi}\frac{\partial[\nabla(U+U^I)\cdot\nabla\overline{u}+\nabla(\overline{U}+\overline{U}^I)\cdot\nabla u]}{\partial\mathbf{e}_r}r\hat{r}\tilde{r}\,\mathrm{d}\theta \\ &-\int_0^{2\pi}[\nabla(U+U^I)\cdot\nabla\overline{u}+\nabla(\overline{U}+\overline{U}^I)\cdot\nabla u]\,\hat{r}\tilde{r}\,\mathrm{d}\theta \\ &-\int_0^{2\pi}[\nabla\tilde{U}(\tilde{r})\cdot\nabla\overline{u}+\nabla\overline{\tilde{U}}(\tilde{r})\cdot\nabla u]\,r\hat{r}\,\mathrm{d}\theta \\ &-\int_0^{2\pi}[\nabla(U+U^I)\cdot\nabla\overline{\tilde{u}}(\tilde{r})+\nabla(\overline{U}+\overline{U}^I)\cdot\nabla\tilde{u}(\tilde{r})]\,r\hat{r}\,\mathrm{d}\theta. \end{aligned} \tag{14}$$

As mentioned at the beginning of this section, the reduced space approach is employed, and hence the variations in state $\tilde{U}$ and adjoint $\tilde{u}$ cannot be arbitrary. Instead, by forcing the first variations of $\mathcal{S}(r,U)$ and $\mathcal{T}(r,U,e)$ to vanish, $\tilde{U}$ is the solution of the so-called incremental forward equation:

$$\int_\Omega\overline{\hat{u}}(\nabla^2\tilde{U}+k^2\tilde{U})\,\mathrm{d}\Omega + \int_{\Gamma_s}\frac{\partial\overline{\hat{u}}}{\partial\mathbf{n}}\left[\tilde{U}+\frac{\partial\left(U+U^I\right)}{\partial\mathbf{e}_r}\tilde{r}\right]\mathrm{d}s - \int_{\Gamma_\infty}\overline{\hat{u}}\left(\frac{\partial\tilde{U}}{\partial r}-\mathrm{i}k\tilde{U}\right)\mathrm{d}s = 0, \quad \forall\hat{u}, \tag{15}$$

and $\tilde{u}$ is the solution of the incremental adjoint equation

$$\int_\Omega\overline{\hat{U}}(\nabla^2\tilde{u}+k^2\tilde{u}+K\tilde{U})\,\mathrm{d}\Omega + \int_{\Gamma_s}\frac{\partial\overline{\hat{U}}}{\partial\mathbf{n}}\left[\tilde{u}+\frac{\partial u}{\partial\mathbf{e}_r}\tilde{r}\right]\mathrm{d}s - \int_{\Gamma_\infty}\overline{\hat{U}}\left(\frac{\partial\tilde{u}}{\partial r}+\mathrm{i}k\tilde{u}\right)\mathrm{d}s = 0, \quad \forall\hat{U}. \tag{16}$$

The corresponding strong form of the incremental forward equation reads

$$\nabla^2\tilde{U}+k^2\tilde{U}=0 \quad \text{in } \Omega, \tag{17a}$$

$$\tilde{U} = -\frac{\partial(U+U^I)}{\partial\mathbf{e}_r}\tilde{r} \quad \text{on } \Gamma_s, \tag{17b}$$

$$\lim_{r\to\infty}\sqrt{r}\left(\frac{\partial\tilde{U}}{\partial r}-\mathrm{i}k\tilde{U}\right)=0. \tag{17c}$$

Similarly, the incremental adjoint equation in the strong form is

$$\nabla^2\tilde{u}+k^2\tilde{u} = -K\tilde{U} \quad \text{in } \Omega, \tag{18a}$$

$$\tilde{u} = -\frac{\partial u}{\partial\mathbf{e}_r}\tilde{r} \quad \text{on } \Gamma_s, \tag{18b}$$

$$\lim_{r\to\infty}\sqrt{r}\left(\frac{\partial\tilde{u}}{\partial r}+\mathrm{i}k\tilde{u}\right)=0. \tag{18c}$$

Unlike the speed method [16], the Banach space setting always guarantees the symmetry of the shape Hessian due to the standard result on symmetry of mixed derivatives in differential calculus [17, 14]. The symmetry of the shape Hessian in (14) is hidden in the last two terms. Our next step is to rewrite them into a form where the symmetry is apparent. In order to do this, we choose $\tilde{r}=\hat{r}$ and $\hat{u}=\tilde{u}(\tilde{r})$ in the incremental forward equation (15). For the incremental adjoint equation (16), we take $\hat{U}=\tilde{U}(\hat{r})$. Then, subtracting the forward equation from the adjoint equation, after some simple integration by parts, gives

$$\int_{\Gamma_s}\frac{\partial(U+U^I)}{\partial\mathbf{e}_r}\frac{\partial\overline{\tilde{u}}(\tilde{r})}{\partial\mathbf{n}}\hat{r}\,\mathrm{d}s=\int_{\Gamma_s}\frac{\partial\overline{\tilde{U}}(\hat{r})}{\partial\mathbf{n}}\frac{\partial u}{\partial\mathbf{e}_r}\tilde{r}\,\mathrm{d}s+\int_\Omega K\overline{\tilde{U}(\hat{r})}\tilde{U}(\tilde{r})\,\mathrm{d}\Omega. \tag{19}$$

Moreover, on Γ_s, we have the following trivial identities:

$$\begin{aligned}
&U+U^I=0 \quad\Rightarrow\nabla(U+U^I)=\frac{\partial(U+U^I)}{\partial\mathbf{n}}\mathbf{n},\\
&u=0 \quad\Rightarrow\nabla u=\frac{\partial u}{\partial\mathbf{n}}\mathbf{n},\\
&\mathbf{e}_r\cdot\mathbf{n}=-\frac{r}{\sqrt{r^2+r^{(1)2}}}\Rightarrow\frac{\partial(U+U^I)}{\partial\mathbf{e}_r}=-\frac{\partial(U+U^I)}{\partial\mathbf{n}}\frac{r}{\sqrt{r^2+r^{(1)2}}},\\
&\Rightarrow\frac{\partial u}{\partial\mathbf{e}_r}=-\frac{\partial u}{\partial\mathbf{n}}\frac{r}{\sqrt{r^2+r^{(1)2}}}.
\end{aligned}$$

Thus, (19) becomes

$$-\int_0^{2\pi}\frac{\partial(U+U^I)}{\partial\mathbf{n}}\frac{\partial\overline{\tilde{u}}(\tilde{r})}{\partial\mathbf{n}}r\hat{r}\,\mathrm{d}\theta=-\int_0^{2\pi}\frac{\partial\overline{\tilde{U}}(\hat{r})}{\partial\mathbf{n}}\frac{\partial u}{\partial\mathbf{n}}r\tilde{r}\,\mathrm{d}\theta+\int_\Omega K\overline{\tilde{U}(\hat{r})}\tilde{U}(\tilde{r})\,\mathrm{d}\Omega. \tag{20}$$

Finally, combining equations (20) and (14) gives the symmetric form of the shape Hessian

$$\begin{aligned}
D^2\mathcal{J}(r;\hat{r},\tilde{r})=&\underbrace{\int_\Omega K[\overline{\tilde{U}(\hat{r})}\tilde{U}(\tilde{r})+\overline{\tilde{U}(\tilde{r})}\tilde{U}(\hat{r})]\,\mathrm{d}\Omega}_{\mathcal{H}_1(r;\hat{r},\tilde{r})}\\
&\underbrace{-\int_0^{2\pi}\left[\frac{\partial\tilde{U}(\hat{r})}{\partial\mathbf{n}}\frac{\partial\overline{u}}{\partial\mathbf{n}}+\frac{\partial\overline{\tilde{U}}(\hat{r})}{\partial\mathbf{n}}\frac{\partial u}{\partial\mathbf{n}}\right]r\tilde{r}\,\mathrm{d}\theta}_{\mathcal{H}_2(r;\hat{r},\tilde{r})}\\
&\underbrace{-\int_0^{2\pi}\left[\frac{\partial\tilde{U}(\tilde{r})}{\partial\mathbf{n}}\frac{\partial\overline{u}}{\partial\mathbf{n}}+\frac{\partial\overline{\tilde{U}}(\tilde{r})}{\partial\mathbf{n}}\frac{\partial u}{\partial\mathbf{n}}\right]r\hat{r}\,\mathrm{d}\theta}_{\mathcal{H}_2(r;\tilde{r},\hat{r})}\\
&\underbrace{-\int_0^{2\pi}\left[\frac{\partial(U+U^I)}{\partial\mathbf{n}}\frac{\partial\overline{u}}{\partial\mathbf{n}}+\frac{\partial(\overline{U}+\overline{U}^I)}{\partial\mathbf{n}}\frac{\partial u}{\partial\mathbf{n}}\right]\hat{r}\tilde{r}\,\mathrm{d}\theta}_{\mathcal{H}_3(r;\hat{r},\tilde{r})}\\
&\underbrace{-\int_0^{2\pi}\frac{\partial[\nabla(U+U^I)\cdot\nabla\overline{u}+\nabla(\overline{U}+\overline{U}^I)\cdot\nabla u]}{\partial\mathbf{e}_r}r\hat{r}\tilde{r}\,\mathrm{d}\theta}_{\mathcal{H}_4(r;\hat{r},\tilde{r})}.
\end{aligned} \tag{21}$$

5. Regularity of the forward and adjoint solutions

In this section, we will justify what we have done in section 4 by studying the well-posedness of the forward and adjoint equations, and the regularity of their solutions. We will assume that the scatterer's surface Γ_s is sufficiently smooth so that the forward and adjoint solutions can be shown to be classical using an integral equation method.

First we introduce the standard surface potentials [11, 18],

$$S\varphi(\mathbf{x}) = 2\int_{\Gamma_s} \Phi(\mathbf{x},\mathbf{y})\varphi(\mathbf{y})\,\mathrm{d}s(\mathbf{y}), \quad \mathbf{x}\in\Gamma_s, \tag{22a}$$

$$D\varphi(\mathbf{x}) = 2\int_{\Gamma_s} \frac{\partial\Phi(\mathbf{x},\mathbf{y})}{\partial\mathbf{n}(\mathbf{y})}\varphi(\mathbf{y})\,\mathrm{d}s(\mathbf{y}), \quad \mathbf{x}\in\Gamma_s, \tag{22b}$$

$$D^*\varphi(\mathbf{x}) = 2\int_{\Gamma_s} \frac{\partial\Phi(\mathbf{x},\mathbf{y})}{\partial\mathbf{n}(\mathbf{x})}\varphi(\mathbf{y})\,\mathrm{d}s(\mathbf{y}), \quad \mathbf{x}\in\Gamma_s, \tag{22c}$$

$$T\varphi(\mathbf{x}) = 2\frac{\partial}{\partial\mathbf{n}(\mathbf{x})}\int_{\Gamma_s} \frac{\partial\Phi(\mathbf{x},\mathbf{y})}{\partial\mathbf{n}(\mathbf{y})}\varphi(\mathbf{y})\,\mathrm{d}s(\mathbf{y}), \quad \mathbf{x}\in\Gamma_s, \tag{22d}$$

where Φ is the zero order Hankel function of the first kind for the (incremental) forward equation(s), namely

$$\Phi(\mathbf{x},\mathbf{y}) = \frac{\mathrm{i}}{4}H_0^1(\mathbf{x}-\mathbf{y}),$$

and the zero order Hankel function of the second kind for the (incremental) adjoint solution(s), i.e.

$$\Phi(\mathbf{x},\mathbf{y}) = -\frac{\mathrm{i}}{4}H_0^2(\mathbf{x}-\mathbf{y}) = -\frac{\mathrm{i}}{4}\overline{H_0^1}(\mathbf{x}-\mathbf{y}).$$

Our analysis needs the following useful result due to Kirsch [19, 20].

Lemma 2. *Let $m\in\mathbb{N}\cup\{0\}$ and $\alpha\in(0,1]$. Then,*

(i) Let $\Gamma_s\in C^{m+1,\alpha}$ if $m\geqslant 1$, and $\Gamma_s\in C^2$ if $m=0$, then:
- *S and D map $C^{m,\alpha}(\Gamma_s)$ continuously into $C^{m+1,\alpha}(\Gamma_s)$.*
- *T maps $C^{m+1,\alpha}(\Gamma_s)$ continuously into $C^{m,\alpha}(\Gamma_s)$.*

(ii) Let $\Gamma_s\in C^{m+2,\alpha}$, then D^* maps $C^{m,\alpha}(\Gamma_s)$ continuously into $C^{m+1,\alpha}(\Gamma_s)$.

Proof. See Kirsch [20] for the proof. □

Note that $C^{m,\alpha}(\Gamma_s)$, provided $\Gamma_s\in C^{m,\alpha}$, denotes the space of m-times differentiable functions whose mth derivative is Hölder continuous with exponent α on Γ_s. If Γ_s is parametrized as in (4), where $r\in C^{m,\alpha}([0,2\pi])$, we define $C^{m,\alpha}(\Gamma_s)$ as the space of all functions φ such that $\varphi(\mathbf{r})\in C^{m,\alpha}([0,2\pi])$. The following corollary follows immediately from the preceding lemma.

Corollary 1. *Let $m\in\mathbb{N}\cup\{0\}$ and $\alpha\in(0,1]$. Suppose $\Gamma_s\in C^{m+1,\alpha}$ if $m\geqslant 1$, and $\Gamma_s\in C^2$ if $m=0$; then, S and D are compact in both $C^{m,\alpha}(\Gamma_s)$ and $C^{m+1,\alpha}(\Gamma_s)$.*

Proof. The proof is trivial by the following two facts.

(i) For $\Gamma_s\in C^{0,1}$ and $i<j$, the embedding from $C^{j,\alpha}$ into $C^{i,\alpha}$ is compact [21].

(ii) For continuous linear operators $L : X \to Y$ and $M : Y \to Z$, the operator ML is compact if either L or M is compact [22].

Now it is obvious that S is compact in $C^{m,\alpha}(\Gamma_s)$ since it maps $C^{m,\alpha}(\Gamma_s)$ continuously into $C^{m+1,\alpha}(\Gamma_s)$ and the continuous embedding from $C^{m+1,\alpha}(\Gamma_s)$ into $C^{m,\alpha}(\Gamma_s)$ is compact. The proofs for other cases are similar. □

A standard approach for solving the (incremental) forward equation(s) using integral equation methods is to look for solution as the combination of the single and double potentials

$$v(\mathbf{x}) = \tilde{D}\varphi(\mathbf{x}) - \mathrm{i}\tilde{S}\varphi(\mathbf{x}), \quad \mathbf{x} \in \mathbb{R}^2 \setminus \Gamma_s, \tag{23}$$

where

$$\tilde{S}\varphi(\mathbf{x}) = \int_{\Gamma_s} \Phi(\mathbf{x}, \mathbf{y})\varphi(\mathbf{y})\, \mathrm{d}s(\mathbf{y}), \quad \mathbf{x} \in \mathbb{R}^2 \setminus \Gamma_s, \tag{24}$$

$$\tilde{D}\varphi(\mathbf{x}) = \int_{\Gamma_s} \frac{\partial \Phi(\mathbf{x}, \mathbf{y})}{\partial \mathbf{n}(\mathbf{y})}\varphi(\mathbf{y})\, \mathrm{d}s(\mathbf{y}), \quad \mathbf{x} \in \mathbb{R}^2 \setminus \Gamma_s. \tag{25}$$

The following extension properties of $\tilde{S}$ and $\tilde{D}$ determine the regularity of the forward and adjoint solutions.

Lemma 3. *Assume $m \in \mathbb{N} \cup \{0\}$ and $\alpha \in (0, 1]$. Let $\Gamma_s \in C^{m+1,\alpha}$ if $m \geqslant 1$, and $\Gamma_s \in C^2$ if $m = 0$. Then,*

(i) $\tilde{S}$ maps $C^{m,\alpha}(\Gamma_s)$ continuously into $C^{m+1,\alpha}\left(\mathbb{R}^2 \setminus \Omega_s\right)$,
(ii) $\tilde{D}$ maps $C^{m+1,\alpha}(\Gamma_s)$ continuously into $C^{m+1,\alpha}\left(\mathbb{R}^2 \setminus \Omega_s\right)$.

Proof. We proceed by induction. The proof for $m = 0$ is done in [18] (theorems 2.17 and 2.23). Now assume that the assertions are true for $m - 1$ and we need to show that they hold for m as well. We begin by the following important identities: $\forall \boldsymbol{x} \in \mathbb{R}^2 \setminus \Omega_s$:

$$\nabla_{\mathbf{x}}\tilde{S}\varphi(\mathbf{x}) = \int_{\Gamma_s} \nabla_{\mathbf{x}}\Phi(\mathbf{x}, \mathbf{y})\varphi(\mathbf{y})\, \mathrm{d}s(\mathbf{y}) = \tilde{S}\left[\frac{\partial(\varphi\boldsymbol{\tau})}{\partial s}\right] - \tilde{D}(\varphi\mathbf{n}) \tag{26}$$

and

$$\nabla_{\mathbf{x}}\tilde{D}\varphi(\mathbf{x}) = \int_{\Gamma_s} \nabla_{\mathbf{x}} \frac{\partial \Phi(\mathbf{x}, \mathbf{y})}{\partial \mathbf{n}(\mathbf{y})}\varphi(\mathbf{y})\, \mathrm{d}s(\mathbf{y}) = k^2\tilde{S}(\varphi\mathbf{n}) + \tilde{\nabla}_{\mathbf{x}}\tilde{S}(\nabla\varphi \cdot \boldsymbol{\tau}), \tag{27}$$

where we have defined the tangent vector $\boldsymbol{\tau} = \frac{\mathrm{d}\mathbf{y}}{\mathrm{d}s}$ and $\tilde{\nabla}_{\mathbf{x}}\varphi = \left(\frac{\partial\varphi}{\partial x_2}, -\frac{\partial\varphi}{\partial x_1}\right)$. We now give the proof for (26) and the proof for (27) follows similarly. Using $\nabla_{\mathbf{x}}\Phi(\mathbf{x}, \mathbf{y}) = -\nabla_{\mathbf{y}}\Phi(\mathbf{x}, \mathbf{y})$, we have

$$\nabla_{\mathbf{x}}\tilde{S}\varphi = -\int_{\Gamma_s} \underbrace{[\nabla_{\mathbf{y}}\Phi(\mathbf{x}, \mathbf{y}) \cdot \tau(\mathbf{y})]}_{\frac{\partial\Phi(\mathbf{x},\mathbf{y})}{\partial s(\mathbf{y})}} \varphi(\mathbf{y})\, \tau(\mathbf{y})\, \mathrm{d}s(\mathbf{y}) - \int_{\Gamma_s} \frac{\partial \Phi(\mathbf{x}, \mathbf{y})}{\partial \mathbf{n}(\mathbf{y})}\varphi(\mathbf{y})\, \mathbf{n}(\mathbf{y})\, \mathrm{d}s(\mathbf{y}).$$

A simple integration by parts yields

$$\int_{\Gamma_s} \frac{\partial \Phi(\mathbf{x}, \mathbf{y})}{\partial s(\mathbf{y})}\varphi(\mathbf{y})\, \tau(\mathbf{y})\, \mathrm{d}s(\mathbf{y}) = -\int_{\Gamma_s} \Phi(\mathbf{x}, \mathbf{y}) \frac{\partial\left[\varphi(\mathbf{y})\, \tau(\mathbf{y})\right]}{\partial s(\mathbf{y})}\, \mathrm{d}s(\mathbf{y}),$$

and this completes the proof of (26). Equation (26) shows that $\nabla_{\mathbf{x}}\tilde{S}\varphi(\mathbf{x})$ maps $C^{m,\alpha}(\Gamma_s)$ continuously into $C^{m,\alpha}\left(\mathbb{R}^2 \setminus \Omega_s\right)$ by the induction hypothesis for $m-1$. This implies that $\tilde{S}\varphi(\mathbf{x})$ maps $C^{m,\alpha}(\Gamma_s)$ continuously into $C^{m+1,\alpha}\left(\mathbb{R}^2 \setminus \Omega_s\right)$. The argument for the second assertion follows similarly. □

The ansatz (23) automatically satisfies the Helmholtz equation and the radiation condition, and hence v is analytic in $\mathbb{R}^2 \setminus \Gamma_s$. What remains is to determine φ that satisfies the boundary condition on the scatterer surface. Thus, the boundary condition determines the space for φ, which in turn suggests the correct space for the solution v by lemma 3. Now, by letting $\mathbf{x}$ approach a point on Γ_s, provided that $\varphi \in C(\Gamma_s)$, and using the standard limiting values on the boundary Γ_s for the single and double potentials [18, 11], the trace of the solution on Γ_s can be written as

$$2v(\mathbf{x}) = (\varphi + D\varphi - \mathrm{i}S\varphi)(\mathbf{x}), \quad \mathbf{x} \in \Gamma_s. \tag{28}$$

The regularity of the forward and incremental forward solutions is now presented.

Theorem 1. *Assume $m \in \mathbb{N} \cup \{0\}$ and $\alpha \in (0, 1]$. Let $\Gamma_s \in C^{m+1,\alpha}$ if $m \geqslant 1$, and $\Gamma_s \in C^2$ if $m = 0$. There hold the following.*

(i) The forward equation (3) is well-posed; in particular, $U \in C^{m+1,\alpha}(\mathbb{R}^2 \setminus \Omega_s)$ and the trace $U|_{\Gamma_s} \in C^{m+1,\alpha}(\Gamma_s)$. Both U and $U|_{\Gamma_s}$ depend continuously on $U^I|_{\Gamma_s}$ in the $C^{m+1,\alpha}$-norm.

(ii) The incremental forward equation (17) is well-posed; in particular, $\tilde{U} \in C^{m,\alpha}(\mathbb{R}^2 \setminus \Omega_s)$, and the trace $\tilde{U}|_{\Gamma_s} \in C^{m,\alpha}(\Gamma_s)$. Both $\tilde{U}$ and $\tilde{U}|_{\Gamma_s}$ depend continuously on $\frac{\partial(U+U^I)}{\partial \mathbf{e}_r}\tilde{r}|_{\Gamma_s}$ in the $C^{m,\alpha}$-norm.

Proof.

(i) Equations (28) and (3*b*) allow us to write

$$(\varphi + D\varphi - \mathrm{i}S\varphi)(\mathbf{x}) = -2U^I|_{\Gamma_s}(\mathbf{x}), \quad \mathbf{x} \in \Gamma_s. \tag{29}$$

Now, $U^I|_{\Gamma_s} \in C^{m+1,\alpha}(\Gamma_s)$ because the restriction of an analytic function on a curve is as smooth as the curve is. By the compactness of S and D in $C^{m+1,\alpha}$ from corollary 1 and the injectivity of $I + D - \mathrm{i}S$ from [11], the Riesz–Fredholm theory [18] tells us that (29) is well-posed in the sense of Hadamard [23], namely, $I+D-\mathrm{i}S : C^{m+1,\alpha}(\Gamma_s) \to C^{m+1,\alpha}(\Gamma_s)$ is bijective and its inverse $(I + D - \mathrm{i}S)^{-1} : C^{m+1,\alpha}(\Gamma_s) \to C^{m+1,\alpha}(\Gamma_s)$ is bounded. As a result, $\varphi \in C^{m+1,\alpha}(\Gamma_s)$, and hence $U \in C^{m+1,\alpha}(\mathbb{R}^2 \setminus \Omega_s)$ by lemma 3. Moreover, $U|_{\Gamma_s} \in C^{m+1,\alpha}(\Gamma_s)$ depends continuously on $-U^I|_{\Gamma_s}$ in the $C^{m+1,\alpha}$-norm. It follows that U depends continuously on $-U^I|_{\Gamma_s}$ as well.

(ii) The proof, which is completely analogous to item (i), is clear from the incremental forward boundary condition (17*b*) and from the result of item (i). □

For the adjoint equations, we first state their representation formulas.

Proposition 1. *The solution(s) of the (incremental) adjoint equation(s) can be represented as*

$$v(\mathbf{x}) = \int_{\Gamma_s} \left[v(\mathbf{y}) \frac{\partial \Phi(\mathbf{x}, \mathbf{y})}{\partial \mathbf{n}(\mathbf{y})} - \Phi(\mathbf{x}, \mathbf{y}) \frac{\partial v(\mathbf{y})}{\partial \mathbf{n}(\mathbf{y})} \right] \mathrm{d}s(\mathbf{y}) - \int_{\Omega} \hat{K}(\mathbf{y}) \Phi(\mathbf{x}, \mathbf{y}) \, \mathrm{d}\Omega, \quad \mathbf{x} \in \mathbb{R}^2, \tag{30}$$

where

$$\hat{K}(\mathbf{y}) = \begin{cases} K(\mathbf{y})[U(\mathbf{y}) - U^{\mathrm{obs}}(\mathbf{y})] & \text{for adjoint equation (9)} \\ K(\mathbf{y})\tilde{U}(\mathbf{y}) & \text{for incremental adjoint equation (18).} \end{cases} \tag{31}$$

Proof. . It is easy by following the proof of the representation theorem for the forward equation [11] and noting that the appearance of the last term is due to the inhomogeneity of the (incremental) adjoint equation(s). □

Proposition 1 suggests that one should look for (incremental) adjoint solution(s) of the form

$$v(\mathbf{x}) = \int_{\Gamma_s} \left[\frac{\partial \Phi(\mathbf{x}, \mathbf{y})}{\partial \mathbf{n}(\mathbf{y})} - \mathrm{i}\Phi(\mathbf{x}, \mathbf{y}) \right] \varphi(\mathbf{y})\, \mathrm{d}s(\mathbf{y}) - \int_{\Omega} \hat{K}(\mathbf{y}) \Phi(\mathbf{x}, \mathbf{y})\, \mathrm{d}\Omega, \quad \mathbf{x} \in \mathbb{R}^2. \tag{32}$$

We are now in the position to address the regularity of the adjoint solutions.

Theorem 2. *Assume $m \in \mathbb{N} \cup \{0\}$ and $\alpha \in (0, 1]$. Let $\Gamma_s \in C^{m+1,\alpha}$ if $m \geqslant 1$, and $\Gamma_s \in C^2$ if $m = 0$. Then, there hold the following.*

(i) The adjoint equation (9) is well-posed; in particular, $u \in C^{m+1,\alpha}(\mathbb{R}^2 \setminus (\Omega_s \cup \Gamma_b))$, and the trace $u|_{\Gamma_s} \in C^{m+1,\alpha}(\Gamma_s)$.

(ii) The incremental adjoint equation (18) is well-posed; in particular, $\tilde{u} \in C^{m,\alpha}(\mathbb{R}^2 \setminus (\Omega_s \cup \Gamma_b))$, and in particular, the trace $\tilde{u}|_{\Gamma_s} \in C^{m,\alpha}(\Gamma_s)$.

Proof. Denote

$$g(\mathbf{x}) = \int_{\Omega} \hat{K}(\mathbf{y}) \Phi(\mathbf{x}, \mathbf{y})\, \mathrm{d}\Omega, \quad \mathbf{x} \in \mathbb{R}^2; \tag{33}$$

then, g satisfies the Helmholtz equation, and hence analytic, in $\mathbb{R}^2 \setminus \Gamma_b$. It follows that the restriction of g on Γ_s, namely $g|_{\Gamma_s}$, belongs to $C^{m+1,\alpha}(\Gamma_s)$.

(i) On the scatterer's surface, again by the standard limiting values of single and double potentials on the boundary Γ_s, we have

$$\varphi + D\varphi - \mathrm{i}S\varphi = 2g|_{\Gamma_s}. \tag{34}$$

As in the proof of theorem 1, we conclude that $u \in C^{m+1,\alpha}(\mathbb{R}^2 \setminus \Omega_s)$ and $u|_{\Gamma_s} \in C^{m+1,\alpha}(\Gamma_s)$.

(ii) The result is clear from the incremental adjoint boundary condition (18*b*) and from the result of item (i).

□

Let us now justify the findings in section 4 in the following theorem.

Theorem 3. *Let $m \in \mathbb{N} \cup \{0\}$ and $\alpha \in (0, 1]$. Suppose $\Gamma_s \in C^{m+1,\alpha}$ if $m \geqslant 1$, and $\Gamma_s \in C^2$ if $m = 0$. Then, the cost functional (2) is twice Gâteaux differentiable. Furthermore, if $m \geqslant 1$, then the cost functional is twice continuously Fréchet differentiable. The shape gradient and shape Hessian are well defined and given in (11) and (21), respectively.*

Proof. It is sufficient to consider two cases: $m = 0$ and $m = 1$. By theorems 1 and 2, if $m = 0$, one has

$$\begin{aligned} U &\in C^{1,1}(\mathbb{R}^2 \setminus \Omega_s), \quad u \in C^{1,1}(\mathbb{R}^2 \setminus (\Omega_s \cup \Gamma_b)), \\ \tilde{U} &\in C^{0,1}(\mathbb{R}^2 \setminus \Omega_s), \quad \tilde{u} \in C^{0,1}(\mathbb{R}^2 \setminus (\Omega_s \cup \Gamma_b)), \end{aligned}$$

where we have taken $\alpha = 1$. This means all derivatives in the shape gradient (11) and shape Hessian (21) exist almost everywhere, and hence are well defined. Furthermore, if $m = 1$, and hence $\Gamma_s \in C^{2,\alpha}$, theorems 1 and 2 additionally imply that they are continuous with respect to r. A similar argument as in the proof of lemma 1 shows that the cost is twice continuously Fréchet differentiable. □

6. Shape Hessian analysis in Hölder spaces

In this section, we use regularity results developed in section 5 to study the shape Hessian. For concreteness, we restricted ourselves to two exemplary cases of the observation operator, namely, the observation is everywhere on a closed curved Γ_b surrounding the obstacle (we call this case continuous observation) and pointwise observation $\Gamma_b = \{x_j^{\text{obs}}\}_{j=1}^{N^{\text{obs}}}$. Unless otherwise stated, we assume $\Gamma_s \in C^{m+1,\alpha}$, $m \geqslant 1$. We begin by studying the first component of the shape Hessian, i.e. $\mathcal{H}_1(r)$, which can be shown to be the Gauss–Newton part of the full Hessian.

If $\Gamma_b \in C^{n,\alpha}$, $n \in \mathbb{N} \cup \{0\}$, the proof of theorem 1 implies that the trace of the incremental forward solution on Γ_b can be identified with the following operator composition:

$$\tilde{U}|_{\Gamma_b} : C^{m+1,\alpha}(\Gamma_s) \ni \hat{r} \mapsto \tilde{U}(\hat{r}) = (D^\circ - \mathrm{i}S^\circ)(I + D - \mathrm{i}S)^{-1} M_1 \hat{r} \in C^{n,\alpha}(\Gamma_b),$$

where

$$M_1 : C^{m+1,\alpha}(\Gamma_s) \ni \mathrm{d}r \mapsto M_1\,\mathrm{d}r = -\frac{\partial\left(U + U^I\right)}{\partial \mathbf{e}_r}\,\mathrm{d}r \in C^{m,\alpha}(\Gamma_s),$$

and

$$S^\circ\varphi(\mathbf{x}) = 2\int_{\Gamma_s} \Phi(\mathbf{x},\mathbf{y})\varphi(\mathbf{y})\,\mathrm{d}s(\mathbf{y}), \qquad \mathbf{x} \in \Gamma_b,$$

$$D^\circ\varphi(\mathbf{x}) = 2\int_{\Gamma_s} \frac{\partial \Phi(\mathbf{x},\mathbf{y})}{\partial \mathbf{n}(\mathbf{y})}\varphi(\mathbf{y})\,\mathrm{d}s(\mathbf{y}), \quad \mathbf{x} \in \Gamma_b.$$

Unlike S and D, S° and D° have non-singular kernels. In fact, they are analytic in both $\mathbf{x}$ and $\mathbf{y}$ owing to $\mathbf{x} \in \Gamma_b$, $\mathbf{y} \in \Gamma_s$ and $\Gamma_b \cap \Gamma_s = \emptyset$. As an immediate consequence, all the properties of S and D apply to S° and D° as well. In particular, the following stronger result holds.

Lemma 4. *Let $\Gamma_s \in C^{m+1,\alpha}$ and $\Gamma_b \in C^{n,\alpha}$; then, S° and D° are linear, bounded and compact maps from $C^{m+1,\alpha}(\Gamma_s)$ to $C^{n,\alpha}(\Gamma_b)$ for all $n \in \mathbb{N} \cup \{0\}$ and $\alpha \in (0, 1]$.*

Proof. We rewrite S° and D° as

$$S^\circ\varphi(\mathbf{x}) = 2\int_0^{2\pi} \Phi(\hat{\mathbf{r}}(\hat{\theta}), \mathbf{r}(\theta))\varphi(\theta)\sqrt{r(\theta)^2 + [r^{(1)}(\theta)]^2}\,\mathrm{d}\theta, \quad \theta \in [0, 2\pi]$$

$$D^\circ\varphi(\mathbf{x}) = 2\int_0^{2\pi} \frac{\partial \Phi(\hat{\mathbf{r}}(\hat{\theta}), \mathbf{r}(\theta))}{\partial \mathbf{n}(\theta)}\varphi(\theta)\sqrt{r(\theta)^2 + [r^{(1)}(\theta)]^2}\,\mathrm{d}\theta, \quad \theta \in [0, 2\pi],$$

where $\mathbf{x} = \hat{r}(\hat{\theta})\mathbf{e}_{\hat{r}}$ with $\hat{r}(\hat{\theta}) \in C^{n,\alpha}[0, 2\pi]$ and $\mathbf{y} = r(\theta)\mathbf{e}_r$ with $r(\theta) \in C^{m+1,\alpha}[0, 2\pi]$. Now it can be observed that differentiation in $\hat{\theta}$ can be interchanged with integration in θ due to the non-singularity and analyticity of the kernels. Moreover, since $\Phi(\cdot, \mathbf{r}(\theta)) \in C^{n,\alpha}[0, 2\pi]$, we have

$$\|S^\circ\varphi\|_{C^{n,\alpha}} \leqslant 4\pi\,\|\Phi(\cdot, \mathbf{r}(\theta))\|_{C^{n,\alpha}}\|\sqrt{r(\theta)^2 + [r^{(1)}(\theta)]^2}\|_\infty\|\varphi\|_\infty, \quad \forall n.$$

A similar result holds for D°, and this ends the proof for the first assertion. The second assertion is simply a direct consequence of the first assertion and the proof of corollary 1. □

Now, it is easy to see that M_1 is continuous due to lemma 5 (to be stated and proved momentarily), and this implies the compactness of $\tilde{U}|_{\Gamma_b}$ owing to the continuity of $(I + D - \mathrm{i}S)^{-1}$ and compactness of $(D^\circ - \mathrm{i}S^\circ)$. Using the definition of the adjoint operator, $\mathcal{H}_1(r; \hat{r}, \tilde{r})$ can be written as

$$\mathcal{H}_1(r; \hat{r}, \tilde{r}) = 2\mathscr{R}(\tilde{U}|_{\Gamma_b}(\hat{r}), \tilde{U}|_{\Gamma_b}(\tilde{r}))_{L^2(\Gamma_b)} = 2\mathscr{R}(\tilde{U}|^*_{\Gamma_b}\tilde{U}|_{\Gamma_b}(\hat{r}), \tilde{r})_{L^2(\Gamma_s)},$$

where $\mathscr{R}$ denotes the real operator which returns the real part of its argument, and $(\cdot)^*$ denotes the adjoint operator. Now the compactness of $\tilde{U}|_{\Gamma_b}$ and $\tilde{U}|^*_{\Gamma_b}$ implies the compactness of $\mathcal{H}_1(r)$.

We have proved the compactness of $\mathcal{H}_1(r)$ for continuous observation. An immediate question that needs to be addressed is whether the same conclusion holds true for pointwise observation as well. The incremental forward solution evaluated at $\mathbf{x}_j^{\text{obs}}$ reads

$$\tilde{U}\left(\hat{r}, \mathbf{x}_j^{\text{obs}}\right) = \int_{\Gamma_s} \underbrace{2\left[\frac{\partial \Phi(\mathbf{x}_j^{\text{obs}}, \mathbf{y})}{\partial \mathbf{n}(\mathbf{y})} - \mathrm{i}\Phi(\mathbf{x}_j^{\text{obs}}, \mathbf{y})\varphi(\mathbf{y})\right]}_{\tilde{\Phi}_j(\mathbf{y})} (I + D - \mathrm{i}S)^{-1} M_1 \hat{r}\, \mathrm{d}s(\mathbf{y})$$

$$= \left(\underbrace{M_1^* \left[(I + D - \mathrm{i}S)^{-1}\right]^*}_{\mathcal{N}} \tilde{\Phi}_j, \hat{r} \right)_{L^2(\Gamma_s)}.$$

Therefore, $\mathcal{H}_1(r; \hat{r}, \tilde{r})$ becomes

$$\mathcal{H}_1(r)[\hat{r}, \tilde{r}] = 2\mathscr{R} \sum_{j=1}^{N^{\text{obs}}} \tilde{U}\left(\hat{r}, \mathbf{x}_j^{\text{obs}}\right) \overline{\tilde{U}}\left(\tilde{r}, \mathbf{x}_j^{\text{obs}}\right)$$

$$= 2\mathscr{R} \left(\left(\sum_{j=1}^{N^{\text{obs}}} \overline{\mathcal{N}}\, \overline{\tilde{\Phi}}_j \mathcal{N} \tilde{\Phi}_j, \hat{r} \right)_{L^2(\Gamma_s)}, \tilde{r} \right)_{L^2(\Gamma_s)}, \tag{35}$$

where $\overline{\mathcal{N}}$ is the complex conjugate of $\mathcal{N}$, i.e. $\overline{N}\varphi = \overline{N\overline{\varphi}}$. Equation (35) shows that the dimension of the range of $\mathcal{H}_1(r)$ is at most N^{obs}. The compactness of $\mathcal{H}_1(r)$ then follows immediately. Thus, we have proved the following result on the compactness of $\mathcal{H}_1(r)$ for both continuous and pointwise observations.

Theorem 4. *The Gauss–Newton component of the Hessian operator, $\mathcal{H}_1(r)$, as a continuous bilinear form on $C^{m+1,\alpha}(\Gamma_s) \times C^{m+1,\alpha}(\Gamma_s)$, is a compact operator.*

In order to study the second component of the shape Hessian, i.e. $\mathcal{H}_2(r)$, we identify the normal derivative of the incremental forward solution with the following operator composition:

$$\left.\frac{\partial \tilde{U}}{\partial \mathbf{n}}\right|_{\Gamma_s} : C^{m,\alpha}(\Gamma_s) \to C^{m-1,\alpha}(\Gamma_s),$$

$$M_1\hat{r} \mapsto \frac{\partial \tilde{U}(M_1\hat{r})}{\partial \mathbf{n}} = \left(\mathrm{i}I - \mathrm{i}D^* + T\right)(I + D - \mathrm{i}S)^{-1} M_1 \hat{r}$$

for $M_1\hat{r} \in C^{m,\alpha}(\Gamma_s)$. This is known as the Dirichlet-to-Neumann (DtN) map [11].

Proposition 2. *The DtN map is one-to-one and onto from $C^{m,\alpha}(\Gamma_s)$ to $C^{m-1,\alpha}(\Gamma_s)$, and its inverse is continuous.*

Proof. The proof that the DtN map is bijective with the bounded inverse from $C^{1,\alpha}(\Gamma_s)$ to $C^{0,\alpha}(\Gamma_s)$ is given in [11]. The extension of the proof to the case of mapping from $C^{m,\alpha}(\Gamma_s)$ to $C^{m-1,\alpha}(\Gamma_s)$ is straightforward with the help of corollary 1, lemma 3, and hence we omit the details here. □

We next prove the following simple lemma.

Lemma 5. *Let $u, v \in C^{m,\alpha}([0, 2\pi])$ and $m \in \mathbb{N} \cup \{0\}$; there hold*

(i) $uv \in C^{m,\alpha}([0, 2\pi])$ and $\|uv\|_{C^{m,\alpha}} \leqslant \|u\|_{C^{m,\alpha}} \|v\|_{C^{m,\alpha}}$
(ii) If $\min_{[0,2\pi]} |u| > \epsilon > 0$, then $\frac{1}{u} \in C^{m,\alpha}([0, 2\pi])$.

Proof.

(i) It is easy to see that if $u, v \in C^{0,\alpha}([0, 2\pi])$, then

$$\|uv\|_{C^{0,\alpha}} \leqslant \|u\|_{C^{0,\alpha}} \|v\|_{C^{0,\alpha}},$$

which in turn implies $uv \in C^{0,\alpha}([0, 2\pi])$ [24]. Now $u, v \in C^{m,\alpha}([0, 2\pi])$ implies $u^{(j)}, v^{(j)} \in C^{0,\alpha}([0, 2\pi]), \forall j \leqslant m$. The proof is now complete by observing that $(uv)^{(k)}$ with $k \leqslant m$ only involves products of the type $u^{(j)}v^{(i)}$ with $i \leqslant k$, $j \leqslant k$, and that the product $\|u\|_{C^{m,\alpha}} \|v\|_{C^{m,\alpha}}$ has more terms than $\|uv\|_{C^{m,\alpha}}$.

(ii) Let $w = 1/u$; then, $l \leqslant |w| \leqslant L$ where $1/l = \max_{[0,2\pi]} |u|$ and $1/L = \min_{[0,2\pi]} |u|$. It is trivial to show that $w \in C^{0,\alpha}([0, 2\pi])$. Now observe that $w^{(k)}$ for $k \leqslant m$ only involves products of three terms w, $u^{(j)}$ and $u^{(i)}$ for $j \leqslant k$, $i \leqslant k$, and this ends the proof. □

It is convenient to denote

$$\zeta_1 = -\frac{\partial(U + U^I)}{\partial \mathbf{e}_r} \in C^{m,\alpha}(\Gamma_s), \quad \zeta_2 = \frac{\partial \overline{u}}{\partial \mathbf{n}} \in C^{m,\alpha}(\Gamma_s).$$

If either ζ_1 or ζ_2 is zero almost everywhere, then $\mathcal{H}_2(r) = 0$, and hence it will not contribute to the full Hessian. On the other hand, if this does not happen, then the following result on $\mathcal{H}_2(r)$ holds.

Theorem 5. *Assume* $\min_{\Gamma_s} |\zeta_1| > \epsilon_1 > 0$, $\min \Gamma_s |\zeta_2| > \epsilon_2 > 0$*; then,* $\mathcal{H}_2(r)$*, as a continuous bilinear form on* $C^{m,\alpha}(\Gamma_s) \times C^{m,\alpha}(\Gamma_s)$*, is not compact.*

Proof. The bilinearity and continuity are trivial by the definition of $\mathcal{H}_2(r)$ in (21) and the property of the DtN map in proposition 2. Now, due to the assumptions on ζ_1 and ζ_2, it is obvious to see that both

$$M_1 : C^{m,\alpha}(\Gamma_s) \ni \mathrm{d}r \mapsto M_1\,\mathrm{d}r = \zeta_1\,\mathrm{d}r \in C^{m,\alpha}(\Gamma_s) \tag{36}$$

and

$$M_2 : C^{m,\alpha}(\Gamma_s) \ni \mathrm{d}r \mapsto M_2\,\mathrm{d}r = \zeta_2 r\,\mathrm{d}r \in C^{m,\alpha}(\Gamma_s) \tag{37}$$

are bijective and have bounded inverses due to lemma 5. On the other hand, the operator $\mathcal{H}_2(r)$ acting on $\hat{r}$ and $\tilde{r}$ can be written as

$$\mathcal{H}_2(r; \hat{r}, \tilde{r}) = 2\mathscr{R}\left(M_1^* \frac{\partial \tilde{U}}{\partial \mathbf{n}}^* (M_2\hat{r}) + M_2 \frac{\partial \tilde{U}}{\partial \mathbf{n}} (M_1\hat{r}), \tilde{r} \right)_{L^2(\Gamma_s)}. \tag{38}$$

As can be observed, both terms in the first argument of the L^2-inner product in (38) are a composition of three bijective operators with bounded inverses, and they are adjoints of each other. As a result, $\mathcal{H}_2(r)$ is bijective with bounded inverse, and hence is not a compact operator. □

In order to study $\mathcal{H}_3(r)$ and $\mathcal{H}_4(r)$, it is convenient to denote

$$\zeta_3 = \frac{\partial(U + U^I)}{\partial \mathbf{n}} \frac{\partial \overline{u}}{\partial \mathbf{n}} \in C^{m,\alpha}(\Gamma_s), \quad \zeta_4 = \frac{\partial[\nabla(U + U^I) \cdot \nabla \overline{u}]}{\partial \mathbf{e}_r} r \in C^{m-1,\alpha}(\Gamma_s),$$

where we have used lemma 5 to conclude that $\zeta_3 \in C^{m,\alpha}(\Gamma_s)$ and $\zeta_4 \in C^{m-1,\alpha}(\Gamma_s)$. If ζ_3 and ζ_4 are zero almost everywhere on Γ_s, then $\mathcal{H}_3(r) = 0$ and $\mathcal{H}_4(r) = 0$, and hence they have no contributions in the full Hessian. On the other hand, if $\mathcal{H}_3$ and $\mathcal{H}_4$ are not trivial, then their mapping properties are given in the following theorem.

Theorem 6. *$\mathcal{H}_3(r)$ and $\mathcal{H}_4(r)$, as continuous bilinear forms on $C(\Gamma_s) \times C(\Gamma_s)$, are not compact. If, in addition, $\min_{\Gamma_s} |\zeta_3| > \epsilon_3 > 0$ and $\min_{\Gamma_s} |\zeta_4| > \epsilon_4 > 0$, then $\mathcal{H}_3(r)$ and $\mathcal{H}_4(r)$ are not compact in $C^{m,\alpha}(\Gamma_s)$ and $C^{m-1,\alpha}(\Gamma_s)$, respectively.*

Proof. The fact that $\mathcal{H}_3(r)$ and $\mathcal{H}_4(r)$ are bilinear and continuous is trivial. On the other hand, their action on $\hat{r}, \tilde{r}$ can be written as

$$\mathcal{H}_3(r; \hat{r}, \tilde{r}) = 2\mathscr{R}\left(\frac{\partial(U + U^I)}{\partial \mathbf{n}} \frac{\partial \overline{u}}{\partial \mathbf{n}} \hat{r}, \tilde{r}\right)_{L^2(\Gamma_s)}, \tag{39}$$

$$\mathcal{H}_4\left(r; \hat{r}, \tilde{r}\right) = 2\mathscr{R}\left(\frac{\partial[\nabla(U + U^I) \cdot \nabla \overline{u}]}{\partial \mathbf{e}_r} r\hat{r}, \tilde{r}\right)_{L^2(\Gamma_s)}. \tag{40}$$

The first arguments of the L^2-inner products in (39) and (40) are multiplication operators on $C(\Gamma_s)$, and hence $\mathcal{H}_3$ and $\mathcal{H}_4$ are not compact due to a result in [25].

Moreover, if $\min_{\Gamma_s} |\zeta_3| > \epsilon_3 > 0$ and $\min_{\Gamma_s} |\zeta_4| > \epsilon_4 > 0$, lemma 5 tells us that $\mathcal{H}_3(r)$ and $\mathcal{H}_4(r)$ are invertible multiplication operators with bounded inverse in $C^{m,\alpha}(\Gamma_s)$ and $C^{m-1,\alpha}(\Gamma_s)$, respectively. Consequently, they are not compact. □

Remark 1. If $m = 0$, and hence $\Gamma_s \in C^2$, results for $\mathcal{H}_1(r)$ and $\mathcal{H}_3(r)$ still hold, but not for $\mathcal{H}_2(r)$ and $\mathcal{H}_4(r)$. It is not clear to us whether the DtN map is still continuously invertible in this case. Nevertheless, if $\alpha = 1$, $\mathcal{H}_4(r)$ is a multiplication operator in $L^p(0, 2\pi)$, $1 \leqslant p < \infty$, and hence not compact in $L^p(0, 2\pi)$ [26].

7. Shape Hessian analysis in Sobolev spaces

The (non-)compactness of the shape Hessian components in section 6 has been carried out in Hölder spaces. This is natural due to our regularity study in section 5. In this section, we briefly show that it is possible to extend most of the results to a Sobolev space setting. To the end of this section, we conventionally use $C^{2,1}$ for $m = \{0, 1\}$ in the expression $C^{m+1,1}$.

We first recall some important mapping properties of surface potentials in Sobolev spaces [19].

Lemma 6. *Let $s \in \mathbb{R}$, $s \geqslant -1/2$, and m be the smallest integer greater or equal to $|s|$.*

(i) Let $\Gamma_s \in C^{m+1,1}$. Then,
- *S and D map $H^s(\Gamma_s)$ continuously into $H^{s+1}(\Gamma_s)$*
- *T maps $H^{s+1}(\Gamma_s)$ continuously into $H^s(\Gamma_s)$.*

(ii) Let $\Gamma_s \in C^{m+2,1}$; then, D^* maps $H^s(\Gamma_s)$ continuously into $H^{s+1}(\Gamma_s)$.

The following compactness result, analogous to corollary 1, is a direct consequence of lemma 6 and the Rellich theorem on compact embeddings of Sobolev spaces [24, 27].

Corollary 2. *Let $s \in \mathbb{R}$, $s \geqslant -1/2$, and m be the smallest integer greater or equal to $|s|$, and $\Gamma_s \in C^{m+1,1}$. Then, S and D are compact in both $H^s(\Gamma_s)$ and $H^{s+1}(\Gamma_s)$.*

Thus, the Riesz–Fredholm theory still holds to deduce that $(I + D - \mathrm{i}S)$ is bijective with continuous inverse in both $H^s(\Gamma_s)$ and $H^{s+1}(\Gamma_s)$, since $(I + D - \mathrm{i}S)$ is injective in $L^2(\Gamma_s)$ [19].

A result similar to lemma 4 reads as follows.

Lemma 7. *Let $s, t \in \mathbb{R}$, $s \geqslant -1/2$, m be the smallest integer greater or equal to $|s|$, and n be the smallest integer greater or equal to $|t|$. Suppose $\Gamma_b \in C^{n,1}$ and $\Gamma_s \in C^{m+1,1}$. Then, S° and D° are linear, bounded and compact maps from $H^s([0, 2\pi])$ to $H^t([0, 2\pi])$ for all $s, t \in \mathbb{R}$, $s \geqslant -1/2$.*

Proof. We present a proof for S° using the Sobolev space theory for periodic functions developed in Kress [24], and the proof for D° follows similarly. Denote

$$\tilde{\Phi}(\hat{\theta}, \theta) = \Phi(\hat{\mathbf{r}}(\hat{\theta}), \mathbf{r}(\theta))\sqrt{r^2(\theta) + [r^{(1)}(\theta)]^2};$$

then, we immediately have $\tilde{\Phi}(\hat{\theta}, \theta) \in C^{n,1}[0, 2\pi] \times C^{n,1}[0, 2\pi]$. As a result, $\tilde{\Phi}(\hat{\theta}, \theta)$ admits a Fourier series, i.e.

$$\tilde{\Phi}(\hat{\theta}, \theta) = \sum_k \sum_j c_{j,k} \mathrm{e}^{\mathrm{i}j\hat{\theta}} \mathrm{e}^{\mathrm{i}k\theta},$$

and its Fourier coefficients decay faster than n-order polynomials in j and than m-order polynomials in k, i.e.

$$\sum_{j,k} j^{2n} |c_{j,k}|^2 < \infty, \quad \sum_{j,k} k^{2m} |c_{j,k}|^2 < \infty. \tag{41}$$

Let us denote $d_k = \frac{1}{2\pi} \int_0^{2\pi} \varphi(\hat{\theta}) \mathrm{e}^{\mathrm{i}k\hat{\theta}} \, \mathrm{d}\hat{\theta}$; then, we have

$$S^\circ \varphi = 4\pi \sum_j \underbrace{\left(\sum_k c_{j,k} d_k \right)}_{T_j} \mathrm{e}^{\mathrm{i}j\theta}.$$

Next using the Cauchy–Schwarz inequality and (41), the linearity and boundedness of S° are readily available such as

$$\|S^\circ \varphi\|_{H^t}^2 = (4\pi)^2 \sum_j \left(1 + j^2\right)^t |T_j|^2 \leqslant (4\pi)^2 \underbrace{\left(\sum_{j,k} \frac{\left(1 + j^2\right)^t |c_{j,k}|^2}{(1 + k^2)^{s'}} \right)}_{<\infty} \underbrace{\left(\sum_k (1 + k^2)^{s'} |d_k|^2 \right)}_{\|\varphi\|_{H^{s'}}^2},$$

where $-1 < s' < -1/2$. The second assertion follows immediately since the embedding from $H^s[0, 2\pi]$ to $H^{s'}[0, 2\pi]$ is compact [24, 27]. □

We next need the mapping properties of the potentials $\tilde{S}$ and $\tilde{D}$ to investigate the DtN map. A result due to Kirsch [19], analogous to lemma 3, states

Lemma 8. *Let $s \in \mathbb{R}$, $s \geqslant -1/2$, and m be the smallest integer greater than or equal to $|s|$.*

(i) If $\Gamma_s \in C^{m+1,1}$, then $\tilde{S}$ can be extended to the bounded linear operator from $H^s(\Gamma_s)$ into $H^{s+3/2}_{\mathrm{loc}}(\overline{\Omega})$.

(ii) If $\Gamma_s \in C^{m,1}$, then $\tilde{D}$ can be extended to the bounded linear operator from $H^s(\Gamma_s)$ into $H^{s+1/2}_{\mathrm{loc}}(\overline{\Omega})$.

Here comes an extension of the DtN map in proposition 2 from Hölder spaces to Sobolev spaces.

Proposition 3. *Let $s \in \mathbb{R}$, $s \geqslant -1/2$, m be the smallest integer greater or equal to $|s|$, and $\Gamma_s \in C^{m+1,1}$. Then, the DtN map is bijective with continuous inverse from $H^s(\Gamma_s)$ to $H^{s-1}(\Gamma_s)$.*

Proof. Using corollary 2 and lemma 8 instead of corollary 1 and lemma 3, the proof follows the same line as the proof of proposition 2. □

We are now in the position to discuss our main results on the (non-)compactness of each component of the full shape Hessian.

Theorem 7. *$s \in \mathbb{R}, s \geqslant -1/2$, m be the smallest integer greater or equal to $|s|$, and $\Gamma_s \in C^{m+1,1}$.*

(i) $\mathcal{H}_1(r)$ *is compact in* $H^s(\Gamma_s)$.

(ii) Assume $\min_{\Gamma_s} |\zeta_1| > \epsilon_1 > 0, \min \Gamma_s |\zeta_2| > \epsilon_2 > 0$*; then,* $\mathcal{H}_1(r)$ *is bijective with continuous inverse in* $H^s(\Gamma_s)$.

(iii) Assume $\min_{\Gamma_s} |\zeta_3| > \epsilon_3 > 0$*; then,* $\mathcal{H}_3(r)$ *is bijective with continuous inverse in* $H^s(\Gamma_s)$.

(iv) Assume $\min_{\Gamma_s} |\zeta_4| > \epsilon_4 > 0$*; then,* $\mathcal{H}_1(r)$ *is bijective with continuous inverse in* $H^{s-1}(\Gamma_s)$.

Consequently, $\mathcal{H}_2(r)$, $\mathcal{H}_3(r)$ *and* $\mathcal{H}_4(r)$ *are not compact.*

Proof. With the above developments, the proofs of these assertions follow exactly the same line as those of theorems 4, 5 and 6.

(i) Theorem 1 and lemma 5 imply that M_1 is a continuous map in $H^s(\Gamma_s)$. Since $(I + D - \mathrm{i}S)$ is continuously invertible due to corollary 2 and $(D^\circ - \mathrm{i}S^\circ)$ is compact due to lemma 8, the compactness of $\mathcal{H}_1(r)$ follows for both continuous and pointwise observations.

(ii) With the assumptions $\min_{\Gamma_s} |\zeta_1| > \epsilon_1 > 0$ and $\min \Gamma_s |\zeta_2| > \epsilon_2 > 0$, M_1 and M_2 are bijective with continuous inverse in $H^s(\Gamma_s)$. Together with the continuous invertibility of the DtN map, we conclude that $\mathcal{H}_2(r)$ is continuously invertible.

(iii) Under the assumption $\min_{\Gamma_s} |\zeta_3| > \epsilon_3 > 0$, $\mathcal{H}_3(r)$ is a bijective multiplication operator with continuous inverse in $H^s(\Gamma_s)$.

(iv) Under the assumption $\min_{\Gamma_s} |\zeta_4| > \epsilon_4 > 0$, $\mathcal{H}_4(r)$ is a bijective multiplication operator with continuous inverse in $H^{s-1}(\Gamma_s)$. □

8. Eigenvalues of the shape Hessian

We have showed that the Gauss–Newton component of the shape Hessian, namely $\mathcal{H}_1(r)$, is compact while others are not. This implies the ill-posedness of the inverse problem (2)–(3*c*), which is now explained in more detail. Suppose we are solving the inverse problem (2)–(3*c*) iteratively using a Newton method. As the iterated shape r is sufficiently close to the optimal shape, all Hessian components are negligible except $\mathcal{H}_1(r)$. That is, one has to invert $\mathcal{H}_1(r)$ in order to obtain the Newton steps. Due to the compactness of $\mathcal{H}_1(r)$, solving for the Newton steps is an example of solving linear equations of the first kind, which is ill-posed (e.g. [11]). The degree of ill-posedness is reflected by the decay of the eigenvalues of $\mathcal{H}_1(r)$. If the eigenvalues decay slowly to zero, the problem is called mildly ill-posed. If the decay is, however, very rapid, the problem is severely ill-posed [11]. This begs for a study on the decay rate of the eigenvalues of $\mathcal{H}_1(r)$. We begin by rewriting $\mathcal{H}_1(r)$ in terms of operator composition as

$$\mathcal{H}_1(r; \hat{r}, \tilde{r}) = 2\mathscr{R}(M_1^* \mathcal{K}[(D^\circ - \mathrm{i}S^\circ)(I + D - \mathrm{i}S)^{-1}]^*(D^\circ - \mathrm{i}S^\circ)(I + D - \mathrm{i}S)^{-1} M_1 \hat{r}, \tilde{r})_{L^2(\Gamma_s)}, \tag{42}$$

for continuous observation, and as

$$\mathcal{H}_1(r;\hat{r},\tilde{r}) = 2\mathscr{R}\left(\left(\sum_{j=1}^{N^{\text{obs}}} \overline{M_1^*[(I+D-\mathrm{i}S)^{-1}]^*\tilde{\Phi}_j} M_1^*[(I+D-\mathrm{i}S)^{-1}]^*\tilde{\Phi}_j, \hat{r}\right)_{L^2(\Gamma_s)}, \tilde{r}\right)_{L^2(\Gamma_s)} \tag{43}$$

for pointwise observation. We now have the following asymptotic result on the decay rate for both continuous and pointwise observations.

Theorem 8. *Assume $m \in \mathbb{N} \cup \{0\}$ and $\alpha \in (0, 1]$. Let $\Gamma_s \in C^{m+1,\alpha}$ if $m \geqslant 1$, and $\Gamma_s \in C^2$ if $m = 0$. Then, the nth eigenvalues of $\mathcal{H}_1(r)$ asymptotically decay as*

$$\lambda_{1,n} = \mathrm{O}\left(\frac{1}{n^{2m+1+\alpha}}\right).$$

Proof. The fact that $\mathcal{H}_1(r)$ is Hermitian and semi-positive definite is clear from (21). In fact, it is positive definite for the continuous observation due to the unique continuation of solutions of the Helmholtz equation. By the analyticity of $\Phi(\mathbf{x}, \mathbf{y})$, $M_1 \in C^{m,\alpha}(\Gamma_s)$ and $\sqrt{r^2 + r'^2} \in C^{m,\alpha}(\Gamma_s)$, equations (42) and (43) show that $\mathcal{H}_1(r) \in C^{m,\alpha}([0, 2\pi] \times [0, 2\pi])$. Using the main theorem in [28] completes the proof. □

Remark 2. It is important to emphasize that the result in theorem 8 is asymptotic, and hence is only valid for sufficiently large n. The decay rate can be improved further if the shape space and M_1 are analytic. In that case, invoking a result in [29] one can conclude that the decay rate is in fact exponential.

9. An analytical example

In this section, we present an analytical example in which eigenvalues can be expressed in terms of Bessel functions and eigenfunctions can be shown to be Fourier modes. Most of the results are elementary but the proofs are long and tedious, so most of the details are omitted to keep the length of the paper reasonable.

We first recall that the plane wave $\mathrm{e}^{\mathrm{i}kx}$ in the positive x-direction can be represented as the superposition of an infinite number of cylindrical waves [30], i.e.

$$\mathrm{e}^{\mathrm{i}kx} = \sum_{N=-\infty}^{\infty} \mathrm{i}^N J_N(kr)\,\mathrm{e}^{\mathrm{i}N\theta}.$$

Next, we assume that the incident wave is one of such cylindrical waves, namely,

$$U^{ic} = J_N(kr)\,\mathrm{e}^{\mathrm{i}N\theta}, \tag{44}$$

which is an analytic function in $\mathbb{R}^2$. We further assume that the synthetic observation data U^{obs}, as the scattered field obtained from a circular scatterer of radius $r = c$, are observed everywhere on a circle of radius $r = b$. Now, we would like to investigate the shape Hessian evaluated at a circular scatterer of radius $r = a < b$.

For incident plane wave, the analytical solution for circular scatterers is standard [30], and one can adapt the derivation easily to obtain the analytical solution for incident cylindrical waves given by (44). In particular, the solution of the forward equation reads

$$U = -\frac{J_N(ka)}{H_N^1(ka)} H_N^1(kr)\mathrm{e}^{\mathrm{i}N\theta},$$

from which the synthetic observation data follows, namely,

$$U^{\text{obs}} = -\frac{J_N(kc)}{H_N^1(kc)} H_N^1(kr) \mathrm{e}^{\mathrm{i}N\theta}.$$

The total field is now readily available as

$$U + U^{ic} = \underbrace{\left[J_N(kr) - \frac{J_N(ka)}{H_N^1(ka)} H_N^1(kr) \right]}_{f_N(kr)} \mathrm{e}^{\mathrm{i}N\theta}.$$

Similarly, the solution of the incremental forward equation can be shown to be

$$\tilde{U}(\tilde{r}) = \sum_{n=-\infty}^{\infty} A_n(\tilde{r}) H_n^1(kr) \mathrm{e}^{\mathrm{i}n\theta},$$

where

$$A_n(\tilde{r}) = \frac{C_N(ka)}{H_n^1(ka)} \frac{1}{\pi} \int_0^{2\pi} \mathrm{e}^{\mathrm{i}(N-n)\theta} \tilde{r}(\theta) \, \mathrm{d}\theta \quad \text{and} \quad C_N(ka) = \frac{\mathrm{i}}{\pi a H_N^1(ka)}.$$

By using a Green function approach, one can show that the analytical solution of the adjoint equation is given by

$$u = \underbrace{B_N \left[J_N(kr) - \frac{J_N(ka)}{H_N^2(ka)} H_N^2(kr) \right]}_{g_N(kr)} \mathrm{e}^{\mathrm{i}N\theta},$$

where

$$B_N = -\frac{\pi kb}{2} \left[\frac{J_N(ka)}{H_N^1(ka)} - \frac{J_N(kc)}{H_N^1(kc)} \right] H_N^1(kb) H_N^2(kb).$$

The final step is to substitute these analytical solutions into the shape Hessian (21). We begin with the Gauss–Newton component $\mathcal{H}_1(a)$. After some simple manipulations, we have

$$\mathcal{H}_1(a) = \sum_{n=-\infty}^{\infty} \lambda_{1,n} \varphi_{nN}(\theta) \varphi_{nN}(\hat{\theta}), \tag{45}$$

where

$$\lambda_{1,n} = \frac{b}{2a^2\pi^4 \left| H_N^1(ka) \right|^2} \frac{\left| H_n^1(kb) \right|^2}{\left| H_n^1(ka) \right|^2}, \tag{46}$$

$$\varphi_{nN}(\theta) = \begin{cases} \cos(N-n)\,\theta \\ \sin(N-n)\,\theta \end{cases}. \tag{47}$$

As can be seen, the eigenfunctions are Fourier modes. In order to understand the eigenvalues we need the following asymptotic results for Bessel functions of large orders [31], i.e. $n \gg 1$:

$$J_n(r) \approx \frac{1}{\sqrt{2\pi n}} \left(\frac{er}{2n} \right)^n, \tag{48a}$$

$$Y_n(r) \approx \frac{2}{\sqrt{\pi n}} \left(\frac{2n}{er} \right)^n. \tag{48b}$$

Since the first term on the right-hand side of (46) does not depend on n, it can be omitted without changing the asymptotic behavior of the eigenvalues. Asymptotically, the eigenvalues can now be estimated as

$$\lambda_{1,n} \approx \left[\frac{Y_n(kb)}{Y_n(ka)} \right]^2 \approx \left(\frac{a}{b} \right)^{2n}. \tag{49}$$

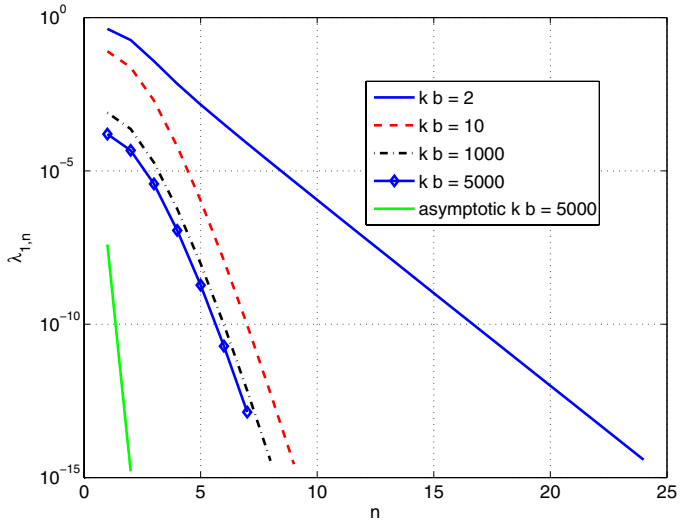

Figure 1. Exponential decay of the eigenvalues of $\mathcal{H}_1(a)$ for $ka = 1$. We show the eigenvalue plots for four different values of observation radius, $kb = \{2, 10, 1000, 5000\}$, together with the asymptotic curve for $kb = 5000$.

Typically $a \ll b$, and (49) implies the exponential decay of $\lambda_{1,n}$ with respect to the index n of the Fourier modes. For this example, it is straightforward to prove the compactness in $L^2(0, 2\pi)$ of the Gauss–Newton component $\mathcal{H}_1(a)$ without using the integral equation method as in sections 6 and 7.

Proposition 4. *$\mathcal{H}_1(a)$ given by (45) is a compact operator in $L^2(0, 2\pi)$.*

Proof. First, the series of eigenvalues converges by the root test. Second, if we form a series of finite-dimensional approximation to $\mathcal{H}_1(a)$ as

$$\mathcal{H}_{1M}(\theta, \hat{\theta}) = \sum_{n=-M}^{M} \lambda_{1,n} \varphi_{nN}(\theta) \varphi_{nN}(\hat{\theta}), \tag{50}$$

then $\mathcal{H}_{1M}(\theta, \hat{\theta})$ is trivially linear and continuous from $L^2(0, 2\pi)$ to $L^2(0, 2\pi)$ by Cauchy–Schwarz inequality and the convergence of the eigenvalue series. That is, $\mathcal{H}_{1M}(\theta, \hat{\theta})$ is compact. Finally, it can be shown that $\mathcal{H}_{1M}(\theta, \hat{\theta})$ converges to $\mathcal{H}_1(a)$ in the operator norm as M approaches infinity, again using the convergence of the eigenvalue series. Hence, $\mathcal{H}_1(a)$ is compact. □

In figure 1, we plot $\lambda_{1,n}$ against the index n in the linear-log scale. Straight lines indicate exponential convergence to zero, in agreement with the estimation (49). Rigorously, the exponential decay in (49) is valid only for large n and this is confirmed for the case $kb = 5000$ in which the asymptotic curve is also plotted. Nevertheless, the decay is very fast so that with $kb = 10$, for example, only nine eigenvalues are sufficient to represent the spectrum of $\mathcal{H}_1(a)$ accurately since the rest of the spectra are below machine zero. Figure 1 also shows that as the observation location is further away from the scatterer, i.e. the observation radius b is larger, the decay is faster, and hence the number of significant eigenvalues is less. We will come back to this point in the later discussion.

For $\mathcal{H}_2(a)$, simple algebra manipulations show that

$$\mathcal{H}_2(a) = \sum_{n=-\infty}^{\infty} \lambda_{2,n}\varphi_{nN}(\theta)\varphi_{nN}(\hat{\theta}),$$

where

$$\lambda_{2,n} = \frac{ka}{2\pi}\mathscr{R}\left[C_N(ka)\frac{\partial g_N(ka)}{\partial r}\frac{H^1_{n-1}(ka) - H^1_{n+1}(ka)}{H^1_n(ka)}\right].$$

Ignoring all the terms independent of n and using the asymptotic formulas (48*a*)–(48*b*) yield

$$\lambda_{2,n} \approx \frac{Y_{n-1}(ka) - Y_{n+1}(ka)}{Y_n(ka)}.$$

Now the estimates

$$\frac{Y_{n+1}(ka)}{Y_{n-1}(ka)} \approx \left(\frac{n+1}{n-1}\right)^{n-3/2}\left[\frac{2(n+1)}{eka}\right]^2,$$
$$\frac{Y_{n+1}(ka)}{Y_n(ka)} \approx \left(\frac{n+1}{n}\right)^{n-1/2}\left[\frac{2(n+1)}{eka}\right],$$
$$\frac{Y_{n-1}(ka)}{Y_n(ka)} \approx \left(\frac{n-1}{n}\right)^{n-3/2}\left(\frac{eka}{2n}\right)$$

imply that $\lambda_{2,n}$ grows with n. As a consequence, $\mathcal{H}_2$ is not compact since the growth of $\lambda_{2,n}$ violates the necessary condition for a self-adjoint operator to be compact.

For $\mathcal{H}_3(a)$ and $\mathcal{H}_4(a)$, it is transparent that they are not compact as follows. Similar to $\mathcal{H}_1(a)$ and $\mathcal{H}_2(a)$, they can be written as

$$\mathcal{H}_3(a) = \sum_{n=-\infty}^{\infty} \lambda_{3,n}\varphi_{n0}(\theta)\varphi_{n0}(\hat{\theta}), \quad \mathcal{H}_4(a) = \sum_{n=-\infty}^{\infty} \lambda_{4,n}\varphi_{n0}(\theta)\varphi_{n0}(\hat{\theta}),$$

where

$$\lambda_{3,n} = 2\pi\mathscr{R}\left(\frac{\partial f_N}{\partial r}\frac{\partial \overline{g}_N}{\partial r}\right), \quad \lambda_{4,n} = 2\pi a\mathscr{R}\left[\frac{\partial\left(\frac{\partial f_N}{\partial r}\frac{\partial \overline{g}_N}{\partial r}\right)}{\partial r}\right].$$

As $\lambda_{3,n}$ and $\lambda_{4,n}$ are constants independent of n, they violate the necessary condition for compactness of $\mathcal{H}_3(a)$ and $\mathcal{H}_4(a)$. As a result, $\mathcal{H}_3(a)$ and $\mathcal{H}_4(a)$ are not compact.

The above example is consistent with the theoretical results in section 6 even though only elementary analytical means are employed here instead of the sophisticated integral equation method. We have shown that the shape Hessian is not compact for non-optimal shapes. However, as a shape approaches an optimal one, the non-compact parts of the shape Hessian, namely, $\mathcal{H}_2(r)$, $\mathcal{H}_3(r)$ and $\mathcal{H}_4(r)$, converge to zero. In that case, the shape Hessian, as a whole, converges to the compact part $\mathcal{H}_1(r)$.

In this example, we have two parameters, namely the incident wave number k and the observation radius b. It is then naturally to ask whether these two parameters can affect the ill-posedness, that is, whether the problem is less or more ill-posed when these parameters change is of interest to us. For this purpose, we, to the end of this section, consider only $\mathcal{H}_1(a)$ and a fixed index n.

9.1. Increase the wave number k

From [31] we have the following asymptotic results as k approaches ∞:

$$J_n(kr) \approx \sqrt{\frac{2}{\pi kr}}\cos(kr - n\pi/2 - \pi/4), \tag{51a}$$

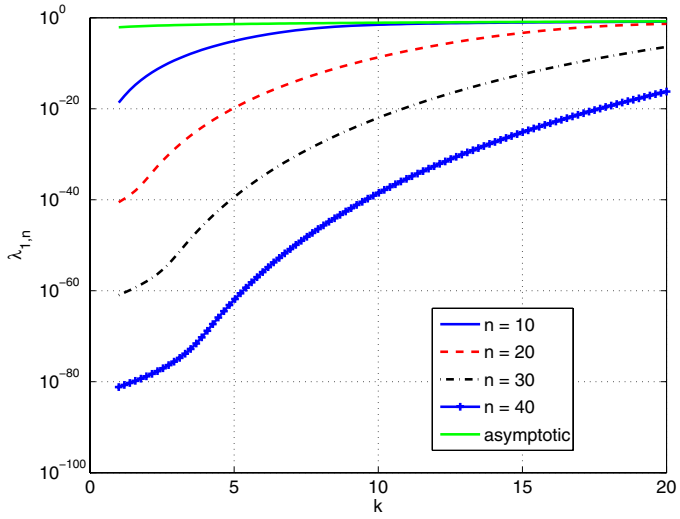

Figure 2. Variations of $\lambda_{1,n}$ for $n = \{10, 20, 30, 40\}$ as k increases from 1 to 20. Other parameters are $a = 1$, $b = 10$ and $N = 2$.

$$Y_n(kr) \approx \sqrt{\frac{2}{\pi kr}} \sin(kr - n\pi/2 - \pi/4). \tag{51b}$$

The eigenvalues in (46) now asymptotically become

$$\lambda_{1,n} \approx \frac{k}{4\pi^3} \quad \text{as} \quad k \to \infty. \tag{52}$$

That is, the eigenvalues tend to be independent of the index n and grow linearly as k increases. This in turns means that $\mathcal{H}_1(a)$ tends to be a non-compact operator. In other words, as $k \to \infty$, the problem of finding Newton steps is continuously invertible in the vicinity of an optimal shape, and hence the ill-posedness due to the compactness of the Hessian is circumvented. However, increasing the wave number induces a different kind of ill-posedness known as the non-uniqueness of stationary shapes or multiple minima phenomenon.

Again, the above result is asymptotic for all n, and we would like to know for each n when the asymptotic behavior is attained. Figure 2 shows $\lambda_{1,n}$ as a function of k for $n \in \{10, 20, 30, 40\}$, $k \in [1, 20]$, $a = 1$, $b = 10$ and $N = 2$. The independence and increase of the index n as predicted by the asymptotic result (52) are clearly demonstrated. As can also be seen, eigenvalues with larger indices (smaller eigenvalues) need a larger wave number to bring them to the asymptotic level. The practical implication here is that while it might be 'easier' to identify the scatterer with a larger wave number, low rank approximation to the $\mathcal{H}_1(r)$ needs more work because the number of dominant eigenvalues grows as k increases.

9.2. Increase the observation radius b

Now let us fix the incident wave number k and allow the observation radius b to vary. The goal is to study the variation of eigenvalues $\lambda_{1,n}$ for a fixed index n. Ignoring all constants independent of b and m and using the asymptotic formulas (51) and (48) yield

$$\lambda_{1,n} \approx b\left|H_n^1(kb)\right|^2 \frac{2}{\pi\left|H_n^1(ka)\right|^2} \approx \frac{2}{\pi\left|H_n^1(ka)\right|^2} \approx \sqrt{\frac{n}{\pi}}\left(\frac{eka}{2n}\right)^n, \quad b \to \infty, \tag{53}$$

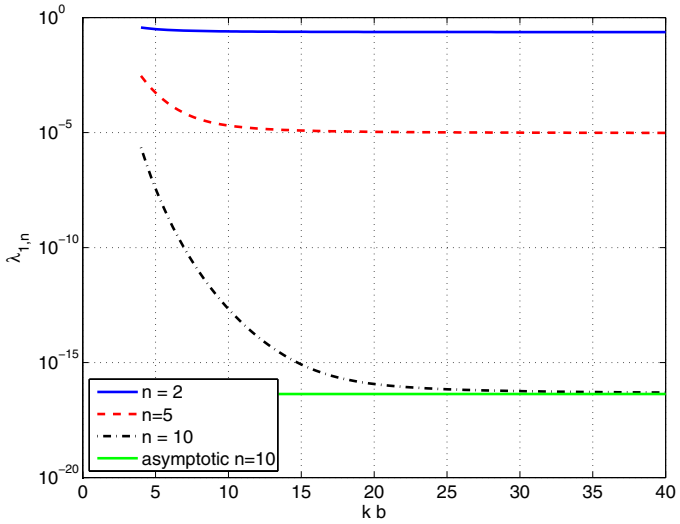

Figure 3. Variations of $\lambda_{1,n}$ with $n \in \{2, 5, 10\}$ as kb increases from 2 to 20 and $ka = 1$. Also shown is the asymptotic value in (53) for $n = 10$.

which decay much faster than those in equation (49) for a fixed but large n. This fact can also be seen in figure 1. We conclude that as the observation radius is larger, the eigenvalues of the Hessian operator decay faster, and hence the problem of finding the Newton steps is more ill-posed. In other words, the number of dominant eigenvalues is less, which is advantageous for low rank approximation of the Gauss–Newton part. It can also be observed in (53) that the eigenvalues become independent of the observation radius b for sufficiently large b.

In figure 3, we compute the exact eigenvalues n from equation (53) (ignoring constants independent of b and n) for $n \in \{2, 5, 10\}$ as kb varies from 2 to 20 and $ka = 1$. The asymptotic value in (53) is confirmed and attained for small b.

9.3. On the assumption $|\zeta_1| > \epsilon_1 > 0, |\zeta_2| > \epsilon_2 > 0$

Finally we would like to check whether this assumption is satisfied in the above example. Simple algebra manipulations show that

$$\zeta_1 = \frac{-2\mathrm{i}}{\pi a H_N^1(ka)} \mathrm{e}^{\mathrm{i}N\theta}, \quad \zeta_2 = \frac{-2\mathrm{i}B_N}{\pi a H_N^2(ka)} \mathrm{e}^{\mathrm{i}N\theta},$$

that is, ζ_2 is zero if kc and ka are zeros of the Bessel function of the first kind J_N. But this cannot happen because both U and U^{obs} would be identically zero in that case.

Recall that the above example is for a cylindrical wave which is a part of the plane wave. As numerically shown in the following, the assumption is also valid for an incident plane wave for which ζ_1 and ζ_2 become

$$\zeta_1 = \sum_{n=-\infty}^{\infty} \frac{2\mathrm{i}^{n+1}\epsilon_N}{\pi a H_N^1(ka)} \mathrm{e}^{\mathrm{i}N\theta}, \quad \zeta_2 = \sum_{n=-\infty}^{\infty} \frac{2\mathrm{i}^{n+1}B_N\epsilon_N}{\pi a H_N^2(ka)} \mathrm{e}^{\mathrm{i}N\theta}.$$

Figure 4 plots ζ_1 and ζ_2 versus θ for the case of $k = 1, a = 1, b = 10, c = 2$. As can be seen, $|\zeta_1| > \epsilon_1 > 0$ and $|\zeta_2| > \epsilon_2 > 0$.

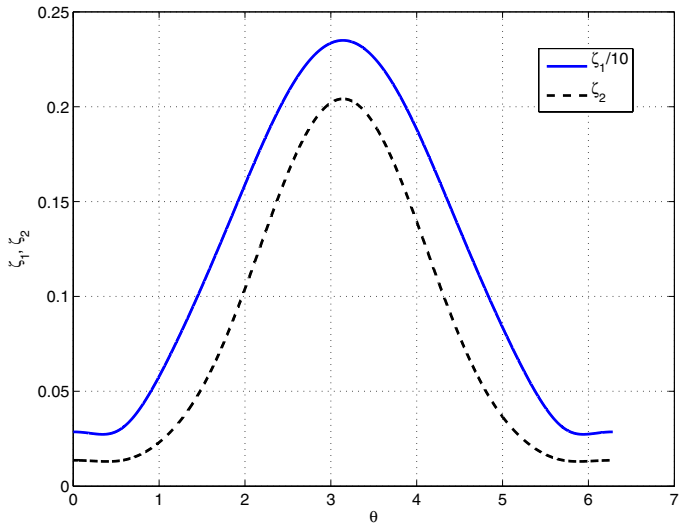

Figure 4. ζ_1 and ζ_2 versus θ for the case of $k = 1$, $a = 1$, $b = 10$, $c = 2$.

10. Numerical results

In this section, we numerically compute the eigenvalues of the shape Hessian (21) to validate our theoretical developments in sections 6 and 7. We choose the Nyström method [11] to discretize the integral equations (29) and (33). Since the normal derivatives of the single and double potentials are required in the incremental forward and adjoint equations, we use the Nyström method of Kress [32] to treat hyper-singular integrals properly.

We consider two shape spaces. The first shape space is analytic and is given by Fourier basis functions:

$$r = \sum_{k=0}^{K} a_k \cos(k\theta) + b_k \sin(k\theta). \tag{54}$$

The second shape space consisting of C^3 shapes is constructed as follows. We use B-spline to fit the above Fourier basis in the least-squares sense and enforce the periodic boundary condition, i.e.

$$r^{(j)}(0) = r^{(j)}(2\pi), \quad j = 0, 1, 2, 3.$$

The Fourier basis functions are sampled sufficiently well so that the original and B-spline fitting results look identical. The difference between the two shape spaces is therefore on $r^{(j)}(\theta)$ for $j \geqslant 1$. Note that we choose C^3 shape space since the Nyström methods in [11, 32] require the third derivative.

For continuous observation, we choose to synthesize the data on the circle centered at the origin with radius $b = 10$, and take unity incident wave number $k = 1$ unless otherwise stated. For pointwise observation, the data are synthesized at 31 points equally distributed in the interval $y \in [-b, b]$ and at $x = -b$. For all examples, we use the trapezoidal rule with 240 points equally distributed in $[0, 2\pi]$ as the numerical quadrature. We are interested in the following drop and kite shapes. The original drop shape reads

$$x = -2\sin(\theta/2) + 1, \quad y = \sin(\theta), \quad t \in [0, 2\pi].$$

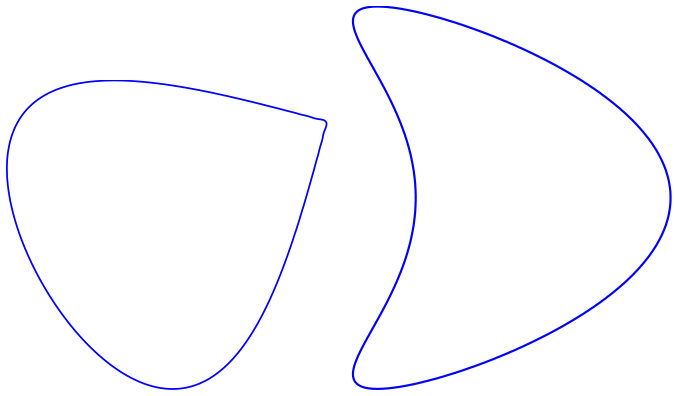

(a) Drop shape geometry (b) Kite shape geometry

Figure 5. Shapes of interest: the drop and kite shapes.

Table 1. Convergence of the Nyström method for the drop geometry.

# Nq	$\mathscr{R}(U_\infty)$	$\mathscr{I}(U_\infty)$
120	−1.285 454 916 526 683	0.307 119 250 858 291
240	−1.285 454 865 187 779	0.307 119 279 365 475
480	−1.285 454 865 187 758	0.307 119 279 365 487

However, the actual drop geometry used in our computations is shown in figure 5(a); a 30 degree rotated version of the original one. Note that we have smoothed out the tip of the drop so that it is a member of the analytic shape space. The kite shape, on the other hand, is given by

$$x = \cos(t) + 0.65\cos(2t) - 0.65, \quad y = 1.5\sin(t), \quad t \in [0, 2\pi],$$

whose geometry is shown in figure 5(b).

In order to show the efficiency of the Nyström method and to verify our implementation, we present a convergence result for the drop shape (a similar convergence of the kite shape is tabulated in [11], and hence omitted here). In particular, we are interested in computing the far field pattern:

$$U_\infty(\hat{\mathbf{x}}) = \frac{e^{-i\frac{\pi}{4}}}{\sqrt{8\pi}} \int_{\Gamma_s} \left(\mathbf{n}(\mathbf{y}) \cdot \hat{\mathbf{x}} + 1\right) e^{-\hat{\mathbf{x}}\cdot\mathbf{y}} \varphi(\mathbf{y})\, ds(\mathbf{y}), \quad \|\hat{\mathbf{x}}\| = 1.$$

We choose $\hat{\mathbf{x}} = (1, 0)$ and show the real together with the imaginary parts of U_∞, namely $\mathscr{R}(U_\infty)$ and $\mathscr{I}(U_\infty)$, versus the number of Nyström quadrature points $\#Nq$ in table 1. As can be observed, the exponential convergence is clearly exhibited, and the result suggests that using 240 quadrature points is enough.

Our goal is to numerically examine the necessary condition for an operator to be compact, namely the convergence of its eigenvalues to zero. If the set of all eigenvalues has a positive lower bound (or negative upper bound), then the operator is not compact. However, even in this case, it is impossible to study all the eigenvalues since they are countably infinite. We will therefore resort to investigate a small dominant part of the spectrum, from which we draw conclusions. In the rest of this section, we 'measure' the degree of ill-posedness by the magnitude of eigenvalues. For example, given two ill-posed inverse problems, i.e. the Hessian

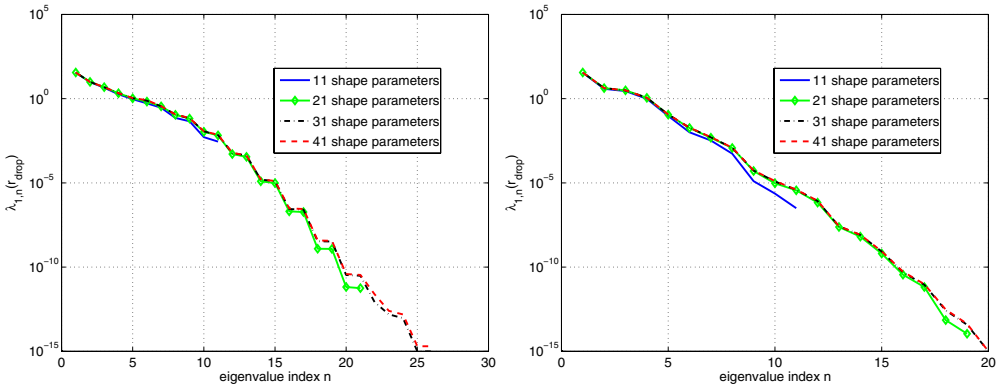

(a) Continuous observation (b) Pointwise observation

Figure 6. Eigenvalues of $\mathcal{H}_1(r_{\text{drop}})$ versus the number of shape parameters using analytic shape space.

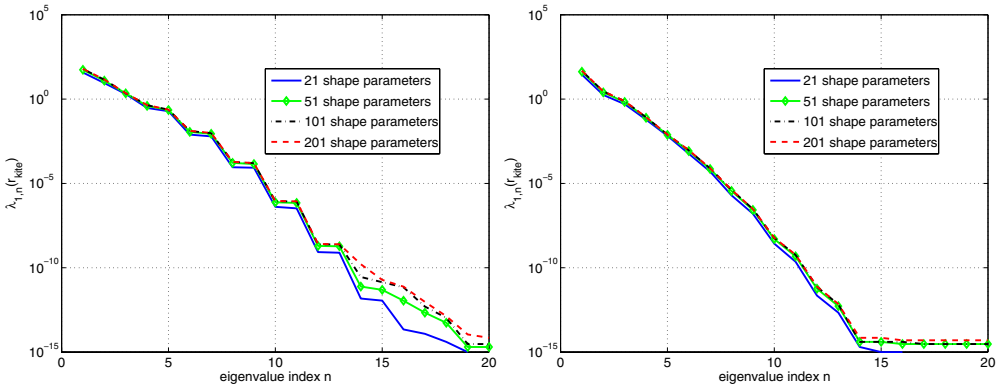

(a) Continuous observation (b) Pointwise observation

Figure 7. Eigenvalues of $\mathcal{H}_1(r_{\text{kite}})$ versus the number of shape parameters using analytic shape space.

eigenvalues decay to zero, we say one problem is more ill-posed than another if the eigenvalues of the former are smaller than those of the latter at the same indices.

Figure 6 shows the eigenvalues of $\mathcal{H}_1(r_{\text{drop}})$ for both continuous and pointwise observations using the analytic shape space. The number of shape parameters is chosen to be $2K-1 \in \{11, 21, 31, 41\}$. As can be seen, the numerical spectrum as a whole converges rapidly and exhibits dimension-independent property. The spectrum for the pointwise observation tends to converge faster than that of the continuous one. One can also draw a similar conclusion for the convergence to zero of the eigenvalues. This is intuitively consistent since the pointwise case is expected to be more ill-posed, i.e. the decay rate of the eigenvalues to zero is faster. Moreover, the linear–log scale in figure 6 shows the exponential decay to zero, agreeing with remark 2.

Similar to figure 6, we plot $\lambda_{1,n}(r_{\text{kite}})$ versus the index n in figure 7 for both continuous and pointwise observations using the analytic shape space. Since the kite shape is non-convex and has small features at the wing tips, the number of shape parameters is expected to be large for

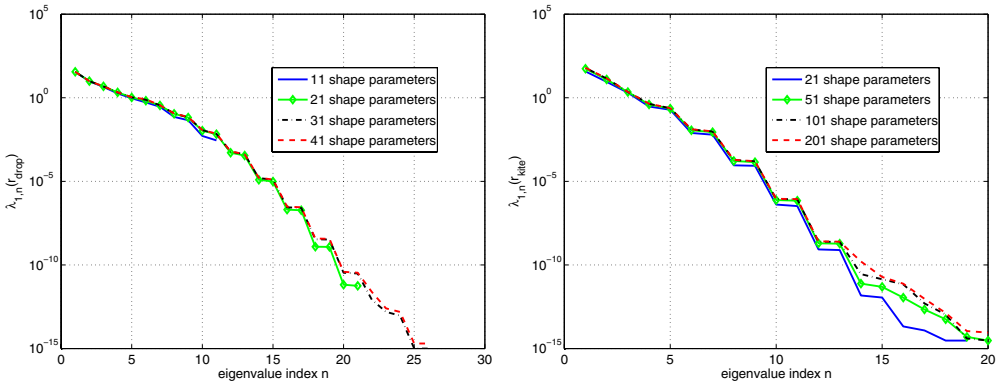

(a) Drop geometry (b) Kite geometry

Figure 8. Eigenvalues of $\mathcal{H}_1(r_{\text{drop}})$ and $\mathcal{H}_1(r_{\text{kite}})$ versus the number of shape parameters using C^3 shape space and continuous observation operator.

the numerical spectrum to converge. This is clearly demonstrated in figure 7 in which we use $2K-1 \in \{21, 51, 101, 201\}$ shape parameters. Compared to figure 6, five times more shape parameters are used, yet the numerical spectrum does not seem to converge for the continuous observation case, especially for small eigenvalues. Since the pointwise observation case is more ill-posed, the convergence is expected to be faster and this is confirmed in figure 7(b). In either case, the compactness of $\mathcal{H}_1(r)$ is clear from the exponential collapsing of eigenvalues to zero on the linear–log scale.

It is of interest to see how the eigenvalues $\lambda_{1,n}$ behave in the less smooth C^3 shape space using continuous observation (similar results are observed for the pointwise observation case, but not presented here). Figure 8 shows that the eigenvalues decay exponentially to machine zero for both the drop and kite geometries and for all numbers of shape parameters under consideration. Note that this does not contradict theorem 8. Instead it suggests that numerical dominant eigenvalues, captured by the shape space under consideration, already converge to machine zero before we can see the asymptotic result predicted by theorem 8. It can be observed that for both geometries, the dominant numerical eigenvalues for C^3 shape space in figures 8(a) and (b) are almost identical to those for analytic shape space in figures 6(a) and 7(a). Since the B-splines are piecewise polynomial, the result indicates that countable discontinuities in higher order derivatives of shape basis functions have insignificant impact on the numerical spectrum.

We next study the variation of $\lambda_{1,n}$ when the observation radius b increases. For convenience, we choose the drop geometry and 41 shape parameters for the analytic shape space. Figure 9(a) shows that for a fixed index n, the corresponding eigenvalue of the continuous observation case decreases initially but then stays constant for sufficiently large b, which is consistent with our analytical result in section 9. For pointwise measurement, however, the eigenvalues, shown in figure 9(b), are observed to decrease constantly as $\mathrm{O}\left(\frac{1}{b}\right)$. This is expected since we lose a factor of b by changing from continuous to pointwise observation as can be seen in (21).

Analogous to section 9, we now study the variation of eigenvalues $\lambda_{1,n}$ when the incident wave number k increases. Again, we choose the drop shape and 41 shape parameters for the analytic shape space. Figure 10 shows that, for a fixed index n, the corresponding eigenvalue increases, in agreement with the result and discussion of section 9. That is, solving for Newton

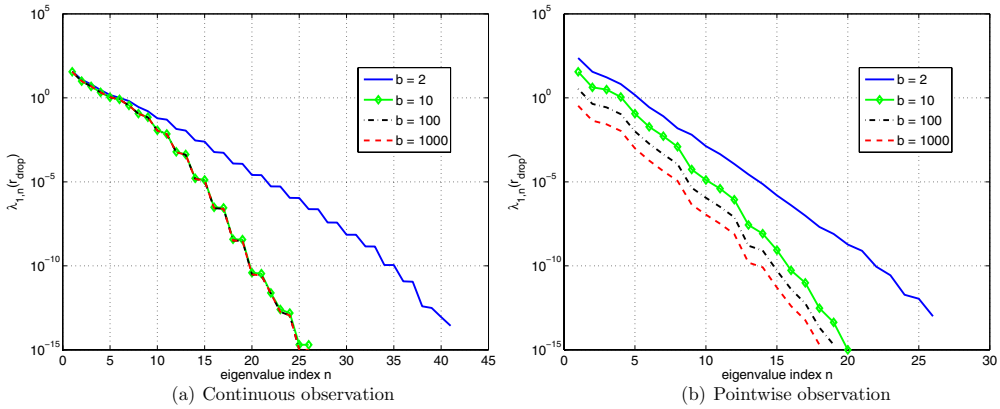

(a) Continuous observation (b) Pointwise observation

Figure 9. Variation of eigenvalues of $\mathcal{H}_1(r_{\text{drop}})$ as the observation radius b increases using analytic shape space.

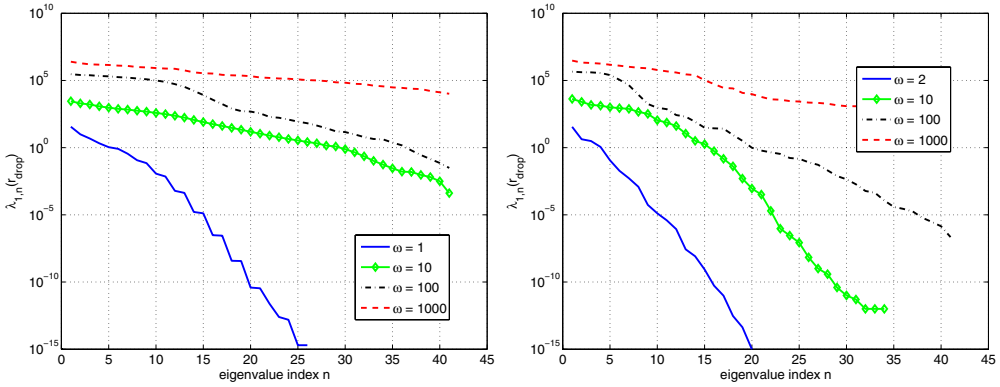

(a) Continuous observation (b) Pointwise observation

Figure 10. Variation of eigenvalues of $\mathcal{H}_1(r_{\text{drop}})$ as the incident wave number k increases using analytic shape space.

steps in the proximity of an optimal shape is less ill-posed as the incident wave number increases.

To the end of this section, we will numerically study the eigenvalues of $\mathcal{H}_2(r)$ and $\mathcal{H}_3(r)$ ($\mathcal{H}_4(r)$ is similar to $\mathcal{H}_3(r)$ and hence omitted). Since the results for continuous and pointwise observations are similar, only the latter will be presented using the analytic shape space. We synthesize observation data from the scattering field of a unit circle centered at the origin, and evaluate the eigenvalues of $\mathcal{H}_2(r)$ and $\mathcal{H}_3(r)$ for both the drop and the kite geometries. Figure 11 plots the numerical spectra of $\mathcal{H}_2(r_{\text{drop}})$ and $\mathcal{H}_2(r_{\text{kite}})$ for various numbers of shape parameters. For all numbers of shape parameters under consideration, the plots suggest the smallest eigenvalue of 0.014 for the drop and 1.7 for the kite. As the number of shape parameters increases, the numerical spectrum resolves more eigenvalues above the smallest eigenvalues. We deduce that $\mathcal{H}_2(r)$ is not compact, in agreement with our analytical results in sections 6 and 7. This validation would be rigorous if we could check all the eigenvalues of $\mathcal{H}_2$, but it is again an impossible task. Hence, we have shown only the trend up to 201 eigenvalues.

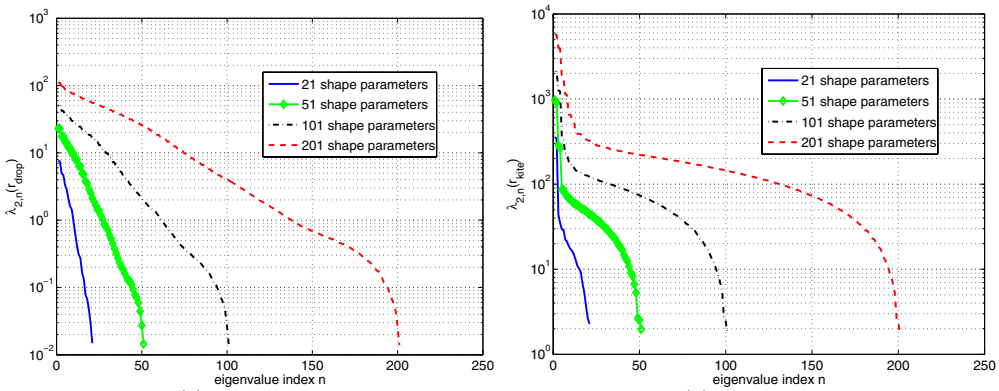

(a) Drop geometry (b) Kite geometry

Figure 11. Eigenvalues of $\mathcal{H}_2(r_{\text{drop}})$ and $\mathcal{H}_2(r_{\text{kite}})$ versus the number of shape parameters using analytic shape space.

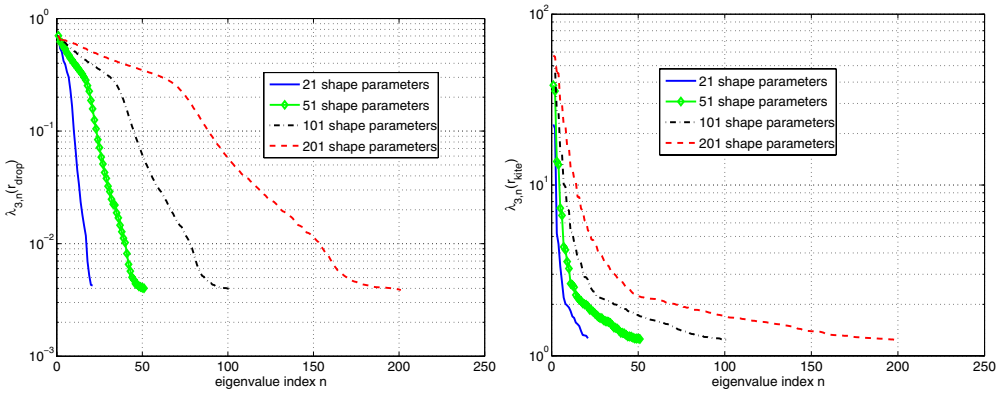

(a) Drop geometry (b) Kite geometry

Figure 12. Eigenvalues of $\mathcal{H}_3(r_{\text{drop}})$ and $\mathcal{H}_3(r_{\text{kite}})$ versus the number of shape parameters using analytic shape space.

Figure 12 is similar to figure 11, but now for $\mathcal{H}_3$. As can be seen, the numerical results validate the non-compactness of $\mathcal{H}_3$ proved in sections 6 and 7. Again, up to 201 shape parameters, the trend of having smallest eigenvalues of 0.004 for the drop and 1.23 for the kite is clear.

It should be pointed out that, unlike the compact Gauss–Newton part, the spectrum of the non-compact parts of the Hessian does not exhibit dimension-independent property.

11. Conclusions

We have presented a shape Hessian analysis for inverse acoustic shape scattering problems. In either Hölder or Sobolev space settings, the shape Hessian is shown to be symmetric and consists of four components, the Gauss–Newton part of which is a compact operator while the others are not. The relationship between the decay rate of the eigenvalues of the Gauss–Newton part and the smoothness of the shape space is presented, which shows that the smoother the

shape space, the faster the decay rate. At the heart of our analysis are the integral equation method, Riesz–Fredholm theory and compact embeddings in Hölder and Sobolev spaces. Analytical and numerical examples are shown to be in agreement with our theoretical results. Ongoing research is to extend our analysis to inverse shape electromagnetic and inverse medium acoustic scattering problems [33, 34]. Our future work also includes application of knowledge of the Hessian and the decaying eigenvalues of the Gauss–Newton part in constructing effective algorithms for inverse shape scattering of acoustic waves.

Acknowledgments

We would like to thank Professor Andreas Kirsch for his generosity in giving us of a copy of his habilitation thesis, without which this article would not have been possible. We also thank Professor Karsten Eppler for sending us a preprint of his paper [13] which was very useful for our developments. This research was supported by AFOSR grant FA9550-09-1-0608; DOE grants DE-SC0002710, DE-FG02-08ER25860, DE-FC52-08NA28615 and DEFC02-06ER25782; and NSF grants CMS-1028889, OPP-0941678, DMS-0724746 and CMS-0619078. The authors would like to thank the anonymous referees for their useful comments and suggestions.

Appendix

In the following, we provide necessary ingredients to extend our theoretical results to three-dimensional scattering problems. To begin, we again identify shapes with their boundaries, but this time for both two and three dimensions in a unified manner. In particular, we assume that the scatterer $\Omega_S \subsetneq \mathbb{R}^d$ for $d = 2, 3$ is a simply connected domain and starlike with respect to the origin. Thus, its boundary $\partial\Omega_S$ can be parametrized as

$$\partial\Omega_S \equiv \Gamma_s = \{\mathbf{r} = r(\boldsymbol{\theta})\mathbf{e}_r : \boldsymbol{\theta} \in \mathbb{S}\},$$

where

$$\boldsymbol{\theta} = \begin{cases} \theta & \text{if } d = 2 \\ (\theta, \psi) & \text{if } d = 3' \end{cases}$$

$$\mathbf{e}_r = \begin{cases} [\cos\theta, \sin\theta]^T & \text{if } d = 2 \\ [\sin\theta\cos\psi, \sin\theta\sin\psi, \cos\theta]^T & \text{if } d = 3 \end{cases}$$

and

$$\mathbb{S} = \begin{cases} [0, 2\pi] & \text{if } d = 2 \\ [0, \pi] \times [0, 2\pi] & \text{if } d = 3' \end{cases}$$

The shape derivatives for the functional $\mathcal{I}$ in (6) can be shown to be

$$D\mathcal{I}(r; \hat{r}) = -\int_{\mathbb{S}} f r \hat{r} g \, \mathrm{d}\boldsymbol{\theta},$$

$$D^2\mathcal{I}(r; \hat{r}, \tilde{r}) = -\int_{\mathbb{S}} \left[\frac{\partial f}{\partial \mathbf{e}_r} + (d-1)\frac{f}{r}\right] r\hat{r}\tilde{r} g \, \mathrm{d}\boldsymbol{\theta},$$

where

$$g = \begin{cases} 1 & \text{if } d = 2 \\ r\sin\theta & \text{if } d = 3' \end{cases}$$

The following useful identities are employed to derive the shape gradient and Hessian:

$$\mathbf{e}_r \cdot \mathbf{n} = -\frac{r}{\overline{n}} \quad \text{and} \quad \mathrm{d}s = g\overline{n} \, \mathrm{d}\boldsymbol{\theta},$$

where

$$\overline{n} = \begin{cases} \sqrt{r^2 + (r^{(1)})^2} & \text{if } d = 2 \\ \sqrt{r^2 + (r_\theta^{(1)})^2 + \left(\dfrac{r_\psi^{(1)}}{\sin\theta}\right)^2} & \text{if } d = 3 \end{cases},$$

where the subscripts θ and ψ denote partial derivatives with respect to θ and ψ, respectively. The fundamental solution of the Helmholtz equation is now given by

$$\Phi(\mathbf{x}-\mathbf{y}) = \begin{cases} \frac{\mathrm{i}}{4} H_0^1(\mathbf{x}-\mathbf{y}) & \text{if } d = 2 \\ \dfrac{1}{4\pi} \dfrac{\mathrm{e}^{\mathrm{i}k|\mathbf{x}-\mathbf{y}|}}{|\mathbf{x}-\mathbf{y}|} & \text{if } d = 3 \end{cases},$$

and the radiation condition can be written as

$$\frac{\partial U}{\partial r} - \mathrm{i}kU = \varphi(r) = o\left(r^{(1-d)/2}\right).$$

With all these prerequisites, it can be verified that the shape gradient and Hessian now read, for $d = 2, 3$,

$$D\mathcal{J}(r;\hat{r}) = -\int_{\mathbb{S}} [\nabla(U+U^I)\cdot\nabla\overline{u} + \nabla(\overline{U}+\overline{U}^I)\cdot\nabla u]\, r\hat{r}\, g\, \mathrm{d}\boldsymbol{\theta},$$

$$\begin{aligned} D^2\mathcal{J}(r;\hat{r},\tilde{r}) = {} & \underbrace{\int_\Omega K[\overline{\tilde{U}(\hat{r})}\tilde{U}(\tilde{r}) + \overline{\tilde{U}(\tilde{r})}\tilde{U}(\hat{r})]\,\mathrm{d}\Omega}_{\mathcal{H}_1(r;\hat{r},\tilde{r})} - \underbrace{\int_{\mathbb{S}} \left[\frac{\partial\tilde{U}(\hat{r})}{\partial\mathbf{n}}\frac{\partial\overline{u}}{\partial\mathbf{n}} + \frac{\partial\overline{\tilde{U}}(\hat{r})}{\partial\mathbf{n}}\frac{\partial u}{\partial\mathbf{n}}\right] r\tilde{r}\, g\,\mathrm{d}\boldsymbol{\theta}}_{\mathcal{H}_2(r;\hat{r},\tilde{r})} \\ & - \underbrace{\int_{\mathbb{S}} \left[\frac{\partial\tilde{U}(\tilde{r})}{\partial\mathbf{n}}\frac{\partial\overline{u}}{\partial\mathbf{n}} + \frac{\partial\overline{\tilde{U}}(\tilde{r})}{\partial\mathbf{n}}\frac{\partial u}{\partial\mathbf{n}}\right] r\hat{r}\, g\,\mathrm{d}\boldsymbol{\theta}}_{\mathcal{H}_2(r;\tilde{r},\hat{r})} \\ & - \underbrace{\int_{\mathbb{S}} (d-1)\left[\frac{\partial(U+U^I)}{\partial\mathbf{n}}\frac{\partial\overline{u}}{\partial\mathbf{n}} + \frac{\partial(\overline{U}+\overline{U}^I)}{\partial\mathbf{n}}\frac{\partial u}{\partial\mathbf{n}}\right]\hat{r}\tilde{r}\, g\,\mathrm{d}\boldsymbol{\theta}}_{\mathcal{H}_3(r;\hat{r},\tilde{r})} \\ & - \underbrace{\int_{\mathbb{S}} \frac{\partial[\nabla(U+U^I)\cdot\nabla\overline{u} + \nabla(\overline{U}+\overline{U}^I)\cdot\nabla u]}{\partial\mathbf{e}_r}\, r\hat{r}\tilde{r}\, g\,\mathrm{d}\boldsymbol{\theta}}_{\mathcal{H}_4(r;\hat{r},\tilde{r})}. \end{aligned}$$

One can also verify that all the results from section 5 to section 7 hold for three-dimensional setting as well with minor adjustments; hence, we omit the details. Results on the decay of eigenvalues of the Gauss–Newton part similar to that of section 8 can be extracted from [35].

References

[1] Eppler K and Harbrecht H 2008 Compact gradient tracking in shape optimization *Comput. Optim. Appl.* **39** 297–318

[2] Eppler K and Harbrecht H 2006 Coupling of FEM–BEM in shape optimization *Numer. Math.* **104** 47–68

[3] Demanet L, Létourneau P-D, Boumal N, Calandra H, Chiu J and Snelson S 2011 Matrix probing: a randomized preconditioner for the wave-equation Hessian arXiv:1101.3615v1 [math.NA]

[4] Flath H P, Wilcox L C, Akçelik V, Hill J, van Bloemen Waanders B and Ghattas O 2011 Fast algorithms for Bayesian uncertainty quantification in large-scale linear inverse problems based on low-rank partial Hessian approximations *SIAM J. Sci. Comput.* **33** 407–32

[5] Bui-Thanh T, Burstedde C, Ghattas O, Martin J, Stadler G and Wilcox L C 2012 Scalable parallel algorithms for uncertainty quantification in high dimensional inverse problems (in preparation)
[6] Chaillat S and Biros G 2012 FaIMS: a fast algorithm for the inverse medium problem with multiple frequencies and multiple sources for the scalar Helmholtz equations (under review)
[7] Björk A 1996 *Numerical Methods for Least Squares Problems* (Philadelphia, PA: SIAM)
[8] Tarantola A 2005 *Inverse Problem Theory and Methods for Model Parameter Estimation* (Philadelphia, PA: SIAM)
[9] Martin J, Wilcox L C, Burstedde C and Ghattas O 2012 A stochastic Newton MCMC method for large scale statistical inverse problems with application to seismic inversion *SIAM J. Sci. Comput.* at press
[10] Bui-Thanh T, Ghattas O and Higdon D 2011 Hessian-informed Gaussian process response surface methods for probability density approximation (submitted)
[11] Colton D and Kress R 1998 *Inverse Acoustic and Electromagnetic Scattering* (*Applied Mathematical Sciences* vol 93) 2nd edn (Berlin: Springer)
[12] Cea J 1980 Problems of shape optimal design *Optimization of Distributed Parameter Structures* ed E J Haug and J Cea (Sijthoff & Noordhoff) pp 1005–48
[13] Eppler K 2000 Second derivatives and sufficient optimality conditions for shape functionals *Control Cybern.* **29** 485–512
[14] Blanchard P and Brüning E 2003 *Mathematical Methods in Physics* (Basel: Birkhäuser)
[15] Kreutz-Delgado K 2009 The complex gradient operator and the CR-calculus *Technical Report UCSD-ECE275CG-S2009v1.0* University of California, San Diego, CA
[16] Delfour M C and Zolésio J-P 2001 *Shapes and Geometries. Analysis, Differential Calculus, and Optimization (Advances in Design and Control)* (Philadelphia, PA: SIAM)
[17] Marsden J E, Abraham R and Ratiu T S 1988 *Manifolds, Tensor Analysis, and Applications* 2nd edn (Berlin: Springer)
[18] Colton D and Kress R 1983 *Integral Equation Methods in Scattering Theory* (New York: Wiley)
[19] Kirsch A 1984 Generalized boundary value- and control problems for the Helmholtz equation *Habilitation Thesis* University of Göttingen
[20] Kirsch A 1989 Surface gradients and continuity properties for some integral operators in classical scattering theory *Math. Methods Appl. Sci.* **11** 789–804
[21] Zeidler E 1986 *Nonlinear Functional Analysis and Its Applications: I. Fixed Point Theorems* (Berlin: Springer)
[22] Tinsley Oden J and Demkowicz L F 2010 *Applied Functional Analysis* (Boca Raton, FL: CRC Press)
[23] Hadamard J 1923 *Lectures on the Cauchy Problem in Linear Partial Differential Equations* (New Haven, CT: Yale University Press)
[24] Kress R 1989 *Linear Integral Equations* (Berlin: Springer)
[25] Singh R K and Summers W H 1987 Compact and weakly compact composition operators on spaces of vector valued continuous functions *Proc. Am. Math. Soc.* vol 99 pp 667–70
[26] Singh R K and Manhas J S 1993 *Composition Operators on Function Spaces (Mathematical Studies)* (Amsterdam: North-Holland)
[27] Cakoni F and Colton D 2006 *Qualitative Methods in Inverse Scattering Theory* (Berlin: Springer)
[28] Cochran J A and Lukas M A 1988 Differentiable positive definite kernels and Lipschitz continuity *Math. Proc. Camb. Phil. Soc.* **104** 361–9
[29] Ganapathi Raman S and Vittal Rao R 1994 Eigenvalues of integral operators on $l^2(i)$ given by analytic kernels *Integr. Eqns Operator Theory* **18** 109–17
[30] Balanis C A 1989 *Advanced Engineering Electromagnetics* (New York: Wiley)
[31] Abramowitz M and Stegun I A (ed) 1965 *Handbook of Mathematical Functions with Formulas, Graphs and Mathematical Tables* (New York: Dover)
[32] Kress R 1995 On the numerical solution of a hypersingular integral equation in scattering theory *J. Comput. Appl. Math.* **61** 345–60
[33] Bui-Thanh T and Ghattas O 2012 Analysis of the Hessian for inverse scattering problems: III. Inverse shape scattering of electromagnetic waves (in preparation)
[34] Bui-Thanh T and Ghattas O 2012 Analysis of the Hessian for inverse scattering problems: II. Inverse medium scattering of acoustic waves *Inverse Problems* **28** 055002
[35] Ferreira J C, Menegatto V A and Peron A P 2008 Integral operators on the sphere generated by positive definite smooth kernels *J. Complexity* **24** 632–47